JGR Atmospheres

RESEARCH ARTICLE

Special Section:
Stratospheric aerosol during the post Pinatubo era: processes , interactions, and impact

Key Points:
- Aerosol size distribution retrievals from Wyoming in situ data are modified to account for laboratory counting efficiency measurements
- Aerosol extinction estimates from the new size distribution retrievals are in good agreement with both SAGE II and HALOE measurements
- Aerosol surface area densities from SAGE II v7.0 agree with the new in situ estimates, which have increased over previous estimates

Correspondence to:
T. Deshler,
deshler@uwyo.edu

Author Contributions:
Conceptualization: Beiping Luo, Thomas Peter, Lars E. Kalnajs
Data curation: Terry Deshler, Mahesh Kovilakam
Formal analysis: Terry Deshler, Beiping Luo, Lars E. Kalnajs
(continued)

Retrieval of Aerosol Size Distributions From In Situ Particle Counter Measurements: Instrument Counting Efficiency and Comparisons With Satellite Measurements

Terry Deshler[1,2] , **Beiping Luo[3]**, **Mahesh Kovilakam[1,4]** , **Thomas Peter[3]**, and **Lars E. Kalnajs[2]**

[1]Department of Atmospheric Science, University of Wyoming, Laramie, WY, USA, [2]Laboratory for Atmospheric and Space Physics, Boulder, CO, USA, [3]Department of Environmental Systems Science, ETH Zurich, Zurich, Switzerland, [4]NASA Langley Research Center, Hampton, VA, USA

Abstract The method to derive aerosol size distributions from in situ stratospheric measurements from the University of Wyoming is modified to include an explicit counting efficiency function (CEF) to describe the channel-dependent instrument counting efficiency. This is motivated by Kovilakam and Deshler's (2015, https://doi.org/10.1002/2015JD023303) discovery of an error in the calibration method applied to the optical particle counter (OPC40) developed in the late 1980s and used from 1991 to 2012. The method can be applied to other optical aerosol instruments for which counting efficiencies have been measured. The CEF employed is the integral of the Gaussian distribution representing the instrument response at any one aerosol channel, the aerosol counting efficiency. Results using the CEF are compared to previous derivations of aerosol size distributions (Deshler et al., 2003, https://doi.org/10.1029/2002JD002514) applied to the measurements before and after Kovilakam and Deshler's correction of number concentration for the OPC40 calibration error. The CEF method is found, without any tuning parameter, to reproduce or improve upon the Kovilakam and Deshler's results, thus accounting for the calibration error without any external comparisons other than the laboratory determined counting efficiency at each aerosol channel. Moments of the new aerosol size distributions compare well with aerosol extinctions measured by Stratospheric Aerosol and Gas Experiment II and Halogen Occultation Experiment in the volcanic period 1991–1996, generally within ±40%, the precision of OPC40 moments, and in the nonvolcanic period after 1996, generally within ±20%. Stratospheric Aerosol and Gas Experiment II and Halogen Occultation Experiment estimates of aerosol surface area are generally in agreement with those derived using the new CEF method.

Plain Language Summary Since 1971, balloon-borne instruments have been used to measure the size distribution of sub-micrometer-sized particles in the stratosphere. These particles, or aerosol, are important for two reasons: (1) They cool the planet by scattering sunlight back to space and (2) they facilitate chemical reactions, which destroy ozone. Ozone shields the Earth from harmful ultraviolet rays from the Sun. Stratospheric aerosol have also been measured from satellites since the 1980s using instruments which measure aerosol extinction, the extent to which sunlight is scattered or absorbed by stratospheric particles. The two measurement methods, satellite- and balloon-borne instruments, have had a long-standing discrepancy between satellite extinction measurements and balloon-borne measurements used to calculate extinction. This paper resolves that discrepancy through laboratory investigations of the counting efficiency of the balloon-borne instruments. When counting efficiency is included in the method to derive aerosol size distribution functions from the balloon-borne measurements, from which extinction and aerosol surface area can be calculated, the two measurement methods are in reasonable agreement. Resolving this discrepancy between the two instruments allows the local balloon-borne measurements to be used for testing the retrieval of aerosol surface area from the global satellite measurements. Stratospheric aerosol surface area is required for global climate models. Thus, this paper provides a basis to characterize the confidence, which can be placed in the global satellite estimates of aerosol surface area for the modeling community.

1. Introduction

The ubiquitous stratospheric aerosol has proven challenging to quantify and to understand. The challenges include sporadic and ill-defined intrusions of source material from large and small volcanic eruptions, a size range and number concentration, which has proven difficult to measure with remote sensing alone, impacts

on radiation and atmospheric chemistry which outweigh their abundance, poorly quantified sources of non-volcanic material from both below and above the stratosphere, and changes in the instruments and methods used to measure the natural abundance (Thomason & Peter, 2006; Kremser et al., 2016). The measurements include global passive (Bourassa et al., 2007; Thomason et al., 2008) and global active (Vernier et al., 2011) satellite instruments, distributed networks of surface active remote sensors (Jäger, 2005; Khaykin et al., 2017), and both campaign and regular aircraft- and balloon-borne in situ measurements (Deshler et al., 2003; Friberg et al., 2014; Jonsson et al., 1995). All of these instruments and platforms have made substantial contributions to the understanding of stratospheric aerosol even though work remains. The focus of this paper is on a reanalysis of the long record of balloon-borne in situ measurements using optical particle counters (OPCs), flown primarily above Laramie, Wyoming, USA (41°N, 106°W; Deshler et al., 2003).

In situ measurements of stratospheric aerosol above Laramie began in 1971 using a two-channel instrument developed and first flown in Minnesota in the 1960s (Rosen, 1964), not long after the initial stratospheric aerosol measurements of Junge et al. (1961). Rosen took his instrument to the University of Wyoming and together with Dave Hofmann made regular in situ aerosol profile measurements above Laramie (Hofmann et al., 1975) and periodic measurements from the tropics to the polar regions in the Western Hemisphere (Rosen et al., 1975). The primary record from this two- to four-channel counter using a scattering angle of 25°, hereafter OPC25, has been summarized by Hofmann (1990, 1993). Spurred by the need to measure polar stratospheric clouds, which contain particles of radii > 0.4 μm at concentrations < 0.001 cm^{-3}, a modified instrument with a flow rate 10 L/min, 10 times the OPC25, and a scattering angle of 40°, hereafter OPC40, was developed in the late 1980s and flown first in Antarctica (Hofmann & Deshler, 1991; Deshler et al., 1994) and subsequently in the Arctic (Deshler & Oltmans, 1998; Deshler et al., 2000). This instrument replaced the OPC25 for flights in Laramie beginning in the early 1990s (Deshler et al., 1993). Deshler et al. (2003) provided a more complete description of this instrument and its application to stratospheric aerosol measurements above Laramie, Wyoming, including comparisons of these in situ measurements with passive extinction measurements from the Stratospheric Aerosol and Gas Experiment (SAGE II) satellite instrument (McCormick et al., 1979). Hervig and Deshler (2002) performed similar comparisons between in situ and remote measurements for the Halogen Occultation Experiment (HALOE; Russell et al., 1993).

During the post Pinatubo period reasonable agreement was found between OPC40 estimates of extinction and SAGE II measurements of extinction and between OPC40 and SAGE II estimates of aerosol surface area density (SAD; Thomason et al., 1997). These agreements, however, were not maintained as the stratosphere relaxed to a nonvolcanically perturbed state in the late 1990s. Then comparisons indicated that the OPC40 estimates of extinction underestimated SAGE II measurements by 50%, while SAGE II underestimated, by 50%, stratospheric aerosol SAD implied by the OPC40 measurements (Deshler et al., 2003; Hervig & Deshler, 2002). Similar results for comparisons between in situ aircraft and SAGE II measurements of aerosol SAD were found by Reeves et al. (2008). The discrepancies in SAD estimates led Thomason et al. (2008) to reevaluate the algorithm used to estimate SAD from SAGE II. The discrepancies in extinction led Kovilakam and Deshler (2015, hereafter KD15), to investigate three possible sources of error in the OPC40 measurements: particle evaporation in the instrument inlet, anisokinetic sampling, and counting efficiency. Pressure dependence in the constant volume flow rate pumps used for the OPC measurements was investigated during the initial instrument design (Hofmann et al., 1975) and more recently (Miao, 2001). Uncertainties on the order of ±5–10% were found with little pressure dependence.

The conclusions of KD15 were as follows: a small pressure- and size-dependent underestimation of the reported particle size due to particle evaporation, minimal effect from anisokinetic sampling, and significant overestimation of the instrument counting efficiency. KD15 developed a model to account for particle evaporation, which, depending on the altitude and size distribution, can lead to an underestimate of aerosol moments by 10–15%. This systematic error was in the right direction but insufficient to explain the underestimation observed. In contrast, the underestimation of the counting efficiency was in the right direction and sufficient to explain the differences observed.

The systematic counting efficiency error resulted from a calibration error, which entered into the standard operating procedures during development of the OPC40. The approach of KD15 to account for the counting efficiency error was to develop an algorithm to increase the number concentration reported at each channel

size. While this approach brought the in situ size distribution estimates of extinction in agreement with SAGE II during the post Pinatubo nonvolcanic period, it caused a somewhat overestimation of SAGE II extinction during the volcanic periods. Thus, KD15's approach was not universal in its impact. Periods of light aerosol loading were more favorably impacted than periods of heavy aerosol loading. The method required an empirically derived parameter, for which SAGE II data were used for comparison. While the results were not heavily dependent on this parameter, there was concern that such a parameter could make the in situ data modestly dependent on SAGE II. Finally, and perhaps most importantly, the method modified the fundamental measurement of the instrument, the aerosol number concentration.

KD15 concluded that the number concentration was lower than the true number concentration at the reported aerosol size. While this is one interpretation of the laboratory counting efficiency measurements, an alternate and stricter interpretation is to say that the size previously reported for each channel of the OPC40 was not correct. While both statements are true, to correct for the first interpretation, and maintain reporting concentrations at the previously reported sizes, requires knowing the true size measured for each channel, and thus a rough aerosol size distribution, which was part of the algorithm of KD15. In contrast, modifying the size reported for each channel, and preserving the number concentration at that channel, is straightforward, although coupling that information to a more realistic counting efficiency for each channel leads to a more complicated algorithm for deriving aerosol size distribution parameters.

For these reasons the laboratory measurements of KD15 are here revisited and used to determine counting efficiency functions (CEFs) to estimate the counting efficiency associated with each channel of the OPC. These new CEF_{ch} for each aerosol channel, specify a new size to be assigned to each OPC channel and are used in a new approach to derive lognormal parameters, which can be used to model the measured aerosol size distribution. Since the calibration of an OPC determines the sizes associated with each aerosol channel, it is appropriate that a calibration error should lead to an adjustment of the size of each aerosol channel rather than an adjustment to the aerosol concentration, which are minimally affected by instrument calibration.

2. Wyoming OPCs—General Description, History, Calibration Procedures

2.1. Instrument Overview and History

Stratospheric aerosol measurements at Laramie, Wyoming, began in 1971 using the instrument developed by Rosen (1964). The instrument uses a broadband incandescent light source and measures the optical scattering from particles passing through the dark field sampling region. The light pulses from aerosol scattering at 25° in the forward direction are focused onto photomultiplier tubes (PMTs) where they are converted to voltage pulses and amplified. The incandescent lamp filament, imaged in the scattering region, is larger than the aerosol sample stream, thus edge effects are not a problem in defining sample volume. Light scattered from particles passing through the beam is collected over a solid angle of 0.15 sr. Two symmetrical independent photon paths are used to limit dark field noise and the influence of cosmic rays. A particle is not accepted unless it produces coincident pulses in both PMTs. Integral particle concentrations are measured by counting coincident PMT pulses, which exceed preset discriminator levels. The instrument is sensitive to optically detectable aerosol as small as 0.15 μm; all sizes are radii. Initial measurements in the 1970s consisted of concentrations of particles >0.15 and 0.25 μm at a sample flow rate of 1 L/min (Hofmann et al., 1975; Rosen et al., 1975). These instruments have been referred to as dustsondes in the past, but here we refer to them as OPC25s after the scattering angle centered at 25°. Due to the forward scattering angle, the counter response function (CRF) has a double valued region between 0.3 and 1.0 μm creating ambiguity. Thus, the instruments were not used for concentrations of particles > 0.3 μm.

The OPC25 design was used to develop an enlarged instrument in the early 1980s to measure low concentrations of large particles produced by the volcanic eruptions of Mt. St. Helens and El Chichón (Hofmann & Rosen, 1982). This required enlarging the sampling inlet and scattering chamber and adding a 50 L/min pump but maintaining the 25° scattering angle. These large-particle counters were flown through 1987 in conjunction with OPC25s. Measurements were limited to particles <0.3 and >1.0 μm by the same ambiguity of instrument response as the OPC25.

In 1989 the OPC25 design was modified: to make measurements in the ambiguous region between 0.3 and 1.0 μm, to increase the number of sizes measured, and to decrease the minimum concentrations measurable.

This development began in response to the need for in situ measurements of polar stratospheric cloud particles >0.3 μm. The scattering angle of the detector axis was increased from 25° to 40° and the flow rate increased from 1 to 10 L/min, with appropriate changes in the inlet design to accommodate this higher flow rate. This new scattering angle allowed unambiguous detection of particles throughout the size range 0.15–10.0 μm. The number of sizes measured was increased to 8 and then 12 channels. The upper channel is determined based on application: 2.0 μm for midlatitude measurements and 10.0 μm for polar stratospheric cloud measurements. Minimum detectable concentrations were increased by a factor of 10 over the 6×10^{-2}-cm^{-3} minimum concentration for the OPC25. These OPCs, hereafter referred to as OPC40, were first used in Antarctica in September 1989 (Hofmann & Deshler, 1991). Calibration flights in Laramie then ensued to insure that the lower sizes measured with the OPC40 were in agreement with the OPC25. Based on this, the OPC40 became the standard instrument in Laramie in 1991 and remained the standard until 2012 (Deshler et al., 2003).

For any single particle counting instrument, such as an OPC, the fundamental measurement is the number concentration of voltage pulses which exceed a preset voltage comparator. The pulse counting rate is converted to particle number concentration using the instrument flow rate. Assigning a size to each pulse measured is based on the instrument calibration and the instrument response function. The instrument, or counter, response function is a model of the voltage pulses expected from particles of known size and index of refraction passing through the sampling chamber. The model depends on instrument optical geometry, light source, detector efficiency, and typically Mie theory. CRFs have been calculated for the OPC25 (Pinnick et al., 1973; Deshler et al., 2003), which clearly display the ambiguous region between 0.3 and 1.0 μm, and for the OPC40 (Hofmann & Deshler, 1991; Deshler et al., 2003), which display the monotonic nature of the OPC40 counter response as a function of size. With an OPC CRF, the levels of the voltage comparators can be set once aerosol size channels are specified.

2.2. OPC Calibration

Calibration amounts to supplying, to the instrument, monodispersed aerosol at a size matching an instrument channel boundary. The comparator level for that channel is then adjusted until half the aerosol pulses are counted at that channel boundary. This becomes the size for 50% counting efficiency. The 50% counting efficiency boundary is used because of several factors, which would cause nonuniform signals from monodispersed aerosol. These include pulse width broadening, variations in light intensity in the scattering region, and asymmetrical scattering to the two PMTs from the aerosol, for example, from aspherical particles. Of these pulse width broadening of the PMTs is the most important based on comparisons between tests of the PMTs with constant light sources and samples using monodispersed aerosol (Eidhammer, 2006; Miao, 2001). Aspherical particles are not of concern for stratospheric sulfuric acid aerosol droplets, the dominant component of stratospheric aerosol, but do arise in polar regions and from meteoritic material. Fortuitously, for a scattering angle of 40° and particles in the size range of 0.1–1.0 μm, there is almost no change in the phase function of oblate or prolate spheroids compared to spheres for aspect ratios from 1.4 to 2.0 (Mishchenko et al., 1996).

The pulse width broadening of PMTs causes even ideal pulses of constant intensity to be spread normally around the delta function, which would ideally represent the pulse distribution from uniform light pulses striking the PMT (Oesburg, 1972; Pinnick & Hofmann, 1973; Sugita et al., 1999). Such broadening was confirmed for the PMTs used in the Wyoming OPCs (Miao, 2001). Thus, for an aerosol exactly at the channel boundary, only half of the particles will generate pulses large enough to be included by the voltage comparator.

For OPC calibration, using monodispersed aerosol selected for each OPC channel, there are two general ways to set the voltage comparator levels: (1) adjust each comparator level voltage until the aerosol counts in the channels below and above the channel boundary are equal and (2) adjust the amplification, gain, applied to the PMT pulses until each comparator level voltage matches the midpoint of the pulse height distribution created from the aerosol stream. Because the voltage pulses expected by OPCs across the size range of 0.1–10.0 μm typically span four orders of magnitude, most OPCs use multiple gain stages to span this range. On a single gain stage the ratio of comparator levels can be set using the ratio of instrument responses expected from the CRF for the sizes to be measured on the gain stage. This requires extensive laboratory measurements to confirm the CRF, as has been done for the OPC40 and OPC25 (Deshler et al., 2003;

Hofmann et al., 1975). Then during calibration, the amplification applied to the PMT for each gain stage is adjusted until one of the aerosol channels on the gain stage matches expectations from the CRF. For the Wyoming OPCs up to four size channels were linked on a single gain stage. Thus, the OPC40 with 12 sizes had three gain stages to be calibrated using method 2 above. The OPC25, with two to four channels had one gain stage.

For other OPCs each channel comparator level is adjusted individually to conform with the pulses received from the calibration aerosol, method 1 above. This is the case for the laser particle counter, which began measurements in Laramie in 2008. Ward et al. (2014) describe this instrument when it was used for polar stratospheric cloud measurements. Some Laramie measurements from this latest instrument are presented in Kremser et al. (2016) and are used for comparison in a paper on volume retrieval from infrared emission measurements (Günther et al., 2018), but this instrument will not be discussed further here. Our interest is in the OPC25 and OPC40, which provide the basis for the measurements from 1971 to 2012. In all cases an OPC calibration is completed by adjusting the gain for a stage until a 50% counting efficiency is reached at the channel selected for calibration. That is 50% of the pulses generated by the instrument from the calibration aerosol are accepted at that channel size. The voltages for other channels in that gain stage are set using the CRF as described above.

The calibration system for the OPC25 was developed in the 1960s before the advent of pulse height analysis (PHA) systems; thus, an analog system was developed, which displayed the number of accepted pulses compared to the total number of particles sampled. The system used the OPC25 CRF for polystyrene latex (PSL) to identify a PSL particle, which mimicked the OPC25 response for a 0.25-μm sulfuric acid and water droplet. The gain on the PMTs was then adjusted until the ratio of the counts on the 0.25-μm channel to the 0.15-μm channel was 0.5, 50% counting efficiency, for the aerosol generated, assuming that all particles were counted in the 0.15-μm channel.

The calibration system for the OPC40 was designed in 1989, simultaneous with the acquisition of a PHA system at Wyoming and with the development of the OPC40, led by T. Deshler shortly after he became involved with the Wyoming in situ measurements. With the availability of a PHA system the calibration system for the OPC40 naturally evolved to include this new capability. Thus, calibration aerosol were selected to match an aerosol channel in the middle of each gain stage and gains were adjusted until the voltage for the calibration aerosol fell at the midpoint of the pulse height distribution measured for the calibration aerosol. This is standard practice for aerosol calibration since it limits the effect of the shape of the pulse height distribution on the calibration (Xu, 2001), and as discussed above. Examples of pulse height distributions from an OPC40 are shown in Figure 1a for sampling 0.45-μm PSL with PMT tube B amplified by the high gain stage and Figure 1b for sampling 1.0-μm PSL with PMT tube A amplified by the low gain stage. As observed the midpoint of each distribution is close to that expected for the calibration aerosol, indicated by the red line and labeled point. Thus, the calibration of these two gain stages for these PMTs was considered complete. The CRF was used to determine the voltage response expected at the PSL size chosen.

The PSL aerosol were created by nebulizing a suspension of PSL in filtered distilled water. Such a system always suffers from small particles which appear as contaminants in even the cleanest water available. The presence of these particles is observed as the peak near 1.0 V in the pulse height distributions shown in Figure 1. A clearer separation of the peak near 1.0 V and the peak of interest near 2 V is observed in Figure 1b than in Figure 1a. In Figure 1b the gain is less on the gain stage measuring 1.0-μm PSL, so the smaller particles produce a smaller signal than on the high gain stage (Figure 1a). The presence of the small contaminant particles does not affect the calibration since the gains are adjusted until the primary peak is centered near the voltage expected from the CRF for the instrument. This procedure of centering the peak is done qualitatively, not quantitatively.

To test the internal consistency of a gain stage for the OPC25 and OPC40, voltage pulses across a range of PSL, which span any one gain stage, were collected and compared to the CRF. With a PHA system such tests are straightforward and have been described and results shown in Deshler et al. (2003), their Figure 2b for the OPC40 and their Figure 2a for a modified OPC25 with two gain stages. Within experimental uncertainty these tests demonstrate the consistency of particle size across the gain stages and between gain stages.
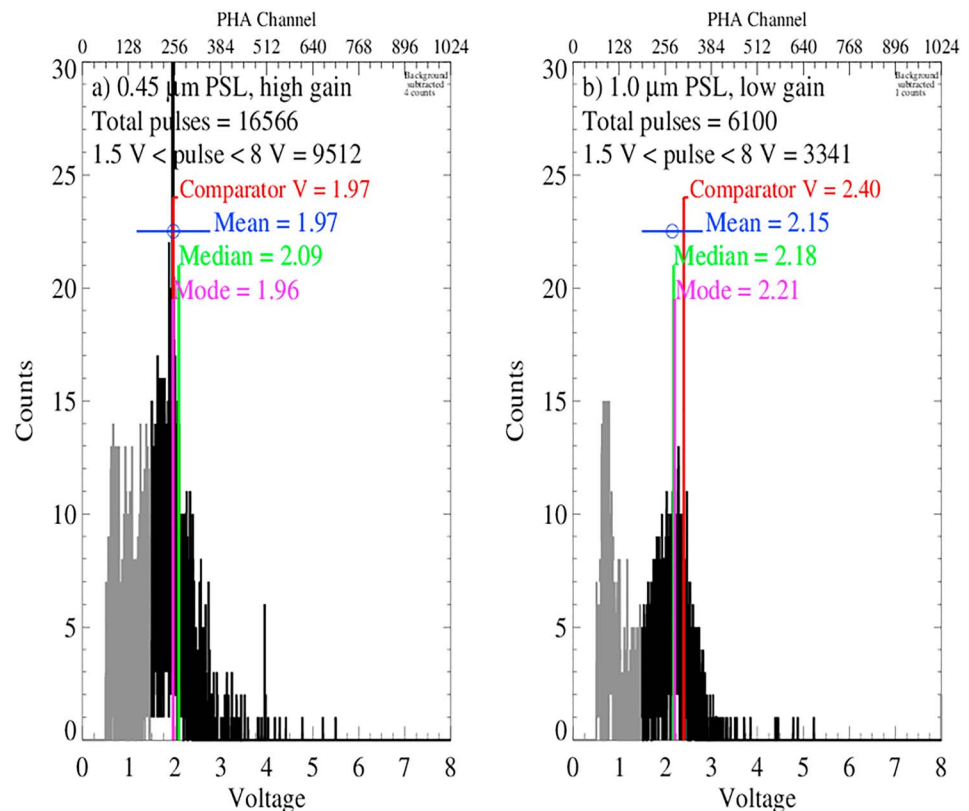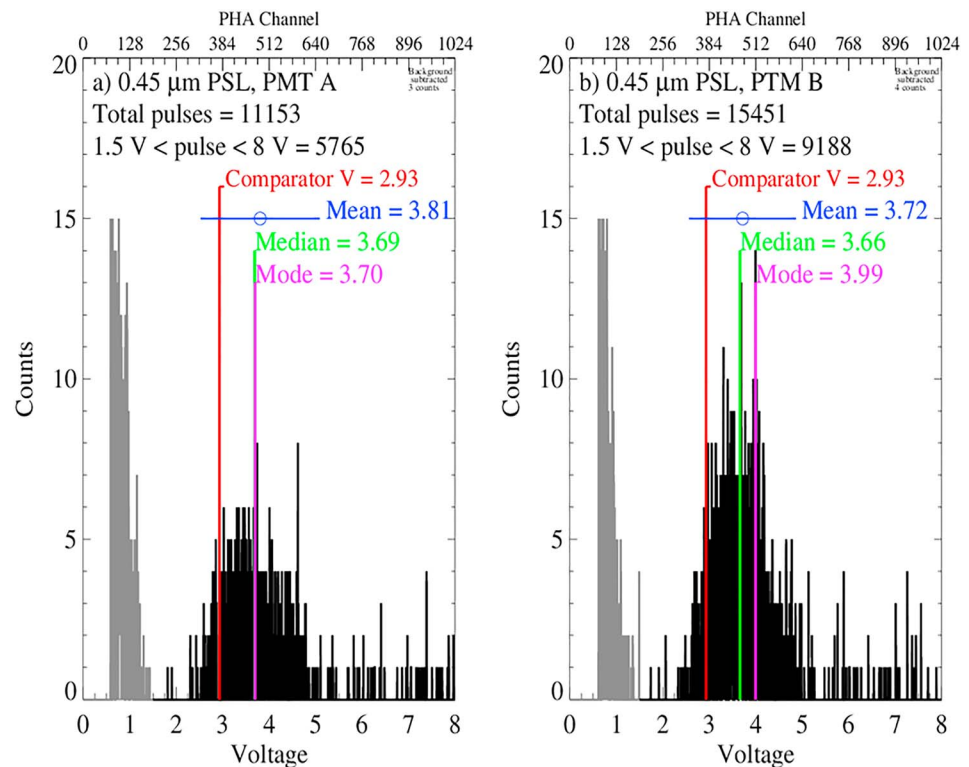
Figure 1. Pulse height distributions from sampling polystyrene latex (PSL) for the calibration of one of the photomultiplier tubes (PMTs) associated with (a) the high gain stage sampling PSL of 0.45 μm and (b) the low gain stage sampling PSL of 1.0 μm. Pulses below 1.5 V are shown in gray to indicate that they primarily arise from small particles formed from contaminants in the water used to aerosolize the PSL. The choice of 1.5 V is somewhat arbitrary and has no impact on the calibration. The comparator voltage, median, and mode of each distribution are indicated with a vertical line and a color-coordinated label. The mean and standard deviation are shown in blue for voltages greater than 1.5 V. The correspondence of the mean and median supports the assumption of a Gaussian distribution.

2.3. OPC Calibration Error

Unappreciated at the time of the development and implementation of the OPC40 calibration procedures using a PHA system (Deshler et al., 2003; Hofmann & Deshler, 1991) was the impact of coincidence counting. The initial development of the OPC25 in the 1960s included just one PMT to convert the scattered light to a voltage pulse. Noise in the measurement, believed to arise from cosmic rays hitting the PMT, led Rosen to add a second PMT focused on the same scattering region. The cosmic ray noise was eliminated by not accepting a particle count unless pulses exceeded the preset threshold from both PMTs (Rosen, 1964; J. M. Rosen, personal communication, 2013). This method also limited the influence of PMT noise. Following the development of the OPC40, all OPC25s were still calibrated using the old analog system because: The system was working fine, it was important to maintain the prior knowledge and a complete link to the measurements between 1971 and 1991, and the OPC25 did not have multiple gain stages. While occasionally the PHA system was used to capture the pulse height distributions from the OPC25, these distributions were not used in the calibration and were ignored. That oversight led to the promulgation of a flawed calibration system for the OPC40.

The design of the OPC40 maintained the OPC25 method to limit cosmic ray and spurious signal noise from the PMTs by retaining two PMTs, each focused on the same scattering region. Each PMT was calibrated as discussed above. An example of the pulse height distribution generated by one PMT from the high gain board when sampling PSL of 0.45-μm radius, and one PMT from the low gain board when sampling PSL of 1.0 μm is shown in Figure 1. The signals below 1.5 V in gray are considered to be the result of very small particles arising from contaminants in the water used to aspirate the PSL. The coincidence of the middle of

Figure 2. Same as Figure 1 but for (a) PMT A and (b) PMT B of an OPC25 calibrated using the analog calibration system. Afte the calibration was complete, the calibration aerosol, 0.45-μm PSL, was used to generate the PMT pulse height distributions shown in the two panels. The 0.45-μm PSL used gives the same counter response as 0.25-μm PSL for an OPC25; see Figure 2 of Deshler et al. (2003). These pulse height distributions for the two PMTs represent any that would have been obtained following the analog calibration of an OPC25. PMT = photomultiplier tube; OPC = optical particle counter; PSL = polystyrene latex.

the distribution with the value expected for each PMT indicates that the gain is properly adjusted for that stage and PMT. Only pulses above the comparator value would be accepted from that PMT by the comparator. The comparator value is calculated based on the CRF and on the particle size selected to coincide with the maximum voltage available on the gain stage, typically 8 V. The second PMT associated with each gain stage was calibrated in a similar manner and would produce similar figures.

The pulse height distribution from an OPC25 calibrated with the old analog system is shown in Figure 2 for the two PMTs of this single gain stage instrument. In this case the pulse height distributions were not used in the calibration but merely checked following calibration. The pulses below 1.5 V from the small particle contaminants in the water used to aerosolize the PSL are apparent. The stronger instrument response, indicated by the higher voltage compared to Figure 1a, reflects the difference in the more forward scattering angle of the OPC25. Because of this, the gain on an OPC25 does not need to be as high as on the OPC40 high gain stage (Figure 1a). Thus, the small contaminant particles appear on an OPC25 at a lower voltage, similar to the OPC40 low gain stage.

While the shape of the pulse height distributions are similar to the OPC40, the comparator value no longer coincides with the middle of the distribution. Rather, approximately 70% of the pulses meet or exceed the PMT comparator value. The reason that the comparator values appear in the analog system below the peaks of the distributions has to do with the coincidence counting requirement. Pulses exceeding the comparator value must occur from both PMTs before a particle is counted. The overall number of pulses accepted by the OPC is then the product of the distributions from each PMT. Thus, for the OPC25, which has individual PMT counting efficiencies of 0.7, the overall counting efficiency is 0.7 * 0.7 = 0.5, which is the 50% counting efficiency desired for an OPC. But for the OPC40 the individual PMT counting efficiencies are set to 0.5, and thus, the overall counting efficiency is 0.5 * 0.5 = 0.25, or a 25% counting efficiency, suggesting an undercounting of a factor of 2.
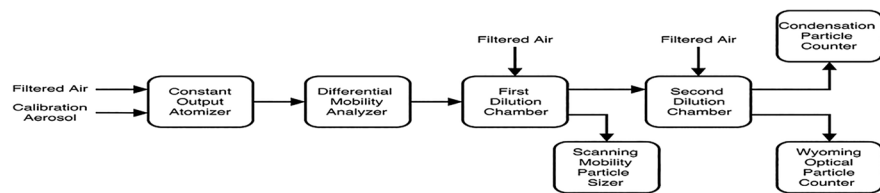
Figure 3. Schematic of laboratory setup for counting efficiency tests. Dried and charge neutralized aerosol from the Atomizer are size selected with the differential mobility analyzer then diluted and tested to confirm the size selected with the scanning mobility particle sizer. The aerosol are then diluted again to achieve concentrations commensurate with stratospheric measurements prior to sampling with a Wyoming optical particle counter and a condensation particle counter.

Achieving a 70% counting efficiency on each PMT to achieve an overall counting efficiency of 50% was built into the analog system used to calibrate the OPC25s before the advent of PHA systems. This requirement was determined empirically and then understood based on the analysis just discussed (Rosen, personal communication, 2013). Somewhere this requirement was lost as the new PHA based calibration system was put into place leading to this deficiency for the OPC40 calibration system.

Realization of this fundamental error motivated the laboratory work of KD15, which confirmed the result. KD15 then went further and proposed modifying the measured number concentration to reflect the more realistic counting efficiency. This approach has several issues discussed above, the most important being that changing the measured aerosol concentration modifies the fundamental measurement of the OPC in flight, which is the number of pulses counted per measurement interval. Coupling this number with the air volume sample per measurement interval provides the aerosol concentration. Instead, we propose here to reanalyze the laboratory measurements of KD15, with several additions to the analysis method, and then to use the new analysis to recommend changes to the size of the aerosol particles sampled by each OPC channel. The method developed here, however, goes beyond just recommending new sizes to be considered as having a 50% counting efficiency. The new method also uses the laboratory work more extensively to map out the size-dependent counting efficiency surrounding each OPC channel, which will then be used to derive new aerosol size distributions from the in situ data.
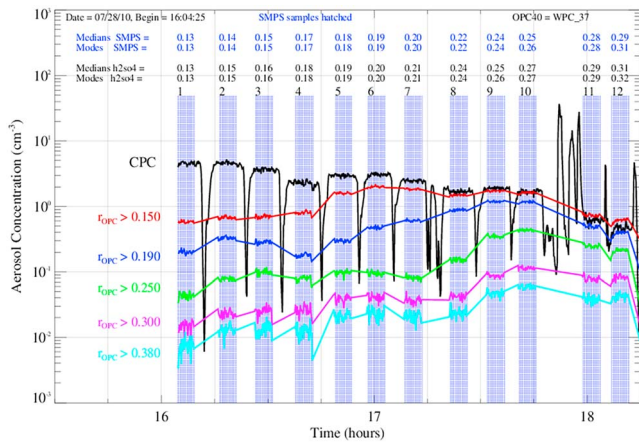
3. Laboratory Measurements of the Counting Efficiency of the OPC40 and OPC25

The analysis of the calibration system for the OPC40 suggested that instead of a 50% counting efficiency at the reported OPC40 sizes, as commonly assumed, the counting efficiency is less, nominally 25%. To confirm this error, KD15 report the results of laboratory measurements of OPC counting efficiencies at a range of aerosol sizes, for each of the OPC channels < 0.3 μm.

3.1. Laboratory Counting Efficiency Measurements

The counting efficiency measurements are completed by generating aerosol of known size and composition and comparing the OPC measurements to simultaneous measurements with a total aerosol counter, in this case a condensation particle counter (CPC). The setup for the laboratory measurements is shown in Figure 3. The aerosol are generated by atomizing a dilute solution of ammonium sulfate using a jet of filtered air. The atomized droplets are dried and charge neutralized before being size sorted using a differential mobility analyzer (DMA). The aerosol are then diluted with filtered air before being tested for size with a scanning mobility particle sizer (SMPS), a scanning DMA. The monodisperse aerosol are then diluted again to reduce concentrations to <10 cm^{-3} before being sampled with an OPC and a CPC. For a particular channel, $N_{ch} = N(r > r_{ch})$ for aerosol channel size r_{ch}, the counting efficiency is the ratio of $N_{ch}(r)$ to $CPC(r)$ for arbitrary aerosol size r.

An example of a test of an OPC40 (WPC_37) is shown in Figure 4. In this case 12 different tests were performed using ammonium sulfate particles between 0.13 and 0.3 μm. The blue hashed areas represent the 5-min time periods when the aerosol generation and sampling instruments were held static. In that period data were collected by an SMPS, to confirm aerosol size, a CPC, and an OPC40 at the nominal radii of 0.15,

Figure 4. Aerosol concentration versus experiment time for laboratory measurements of the counting efficiency for the OPC40 labelled WPC_37 at 13 sizes of ammonium sulfate particles between 0.12 and 0.3 μm. The blue hashed areas are 5-min time periods when the aerosol generation and sampling instruments were held static. The data collected in each 5-min period are: size distribution with an SMPS, total aerosol concentration, N_{CPC}, with a CPC, black line, size spectra with an OPC40 at the nominal radii of 0.15, red, 0.19, blue, 0.25, green, 0.3, magenta, and 0.38 μm, cyan. At the top in blue are the median and mode radii obtained from the SMPS data. Below the median and mode radii from the SMPS are the effective sizes of a sulfuric acid and water droplet, which would generate the same OPC40 counter response as the generated ammonium sulfate. The equivalent sulfuric acid and water radii are calculated based on the OPC40 counter response curves for ammonium sulfate, index of refraction = 1.53, and sulfuric acid and water, index of refraction = 1.45 (*Deshler* et al., 2003). SMPS = scanning mobility particle sizer; OPC = optical particle counter; CPC = condensation particle counter.

0.19, 0.25, 0.3, 0.38 μm. At the top of the figure in blue are listed the median and mode radii as obtained from the 5-min SMPS sample of the ammonium sulfate generated and size selected. Below these median and mode radii are the radii of the equivalent sulfuric acid and water droplet, which would generate the same OPC40 counter response as the measured ammonium sulfate. The correspondences between the sizes of ammonium sulfate and sulfuric acid and water are calculated based on the OPC40 counter response curves for ammonium sulfate, index of refraction = 1.53, and sulfuric acid and water, index of refraction = 1.45 (Deshler et al., 2003). The counting efficiency of each OPC channel is then calculated as the ratio of $N_{ch} : N_{CPC}$, for ch = 1 to 4. Each generated size, r, will provide a counting efficiency for each of the first four channels of the OPC40 at the size of r.

The counting efficiencies implied from the experiments illustrated in Figure 4 cannot be used directly but must be reduced slightly to account for the artifacts of multiply charged particles, which arise when using electrical mobility to select a monodispersed aerosol sample. While the majority of particles entering the DMA from the first charge neutralizer are singly charged, there is a small fraction which contain multiple charges with the fraction decreasing as the number of charges increases from two (Baron & Willeke, 2005). Typically, the fraction of quadruply charged particles is unobservable, but the doubly and triply charged particles are easily observed in the SMPS used to confirm the size of the particles selected by the DMA. Prior to entering the SMPS, used to confirm particle size, the aerosol sample is again charge neutralized; thus, the previously multiply charged particles exiting the DMA are now singly charged. In the SMPS sample these particles appear at their true size, 2 or 3 times as large as the size selected. These large, now singly charged, particles affect the counting efficiency measurements in two ways. First, they alter the median and mean of the SMPS measured distribution away from the size selected, which is best represented by the mode radius. Second, they artificially inflate the counting efficiency measured. Consider an aerosol size selected just below an OPC channel boundary. Less than 50% of the particles at the mode radius selected would be counted by the OPC; however, nearly all the doubly and triply charged particles exiting the DMA, which are larger than the OPC channel boundary, would be counted. Thus, the counting efficiency measured, $CE_{Measured} = N_{ch}/N_{CPC}$, is inflated above the true counting efficiency (CE_{ch}) for the OPC channel at the laboratory aerosol defined by r_{mode}. The large particles above the channel boundary must be subtracted from both the OPC and CPC counts. This was done by correcting the counting efficiency measured to obtain $CE_{ch}(r_{mode})$ as follows:

$$CE_{ch}(r_{mode}) = \left[{N_{ch}}\Big/{N_{CPC}} - {\int_{r_{mode}+3\sigma}^{\infty} CEF_{ch}(r)\frac{dn}{dr}dr}\Big/{N_{CPC}} \right] \times \left[\frac{N_{CPC}}{N_{CPC} - \int_{r_{mode}+3\sigma}^{\infty} \frac{dn}{dr}dr} \right]$$

The first term in brackets, $CE_{Measured}$, is from the experiments displayed in Figure 4, r_{mode} and σ describe the Gaussian distribution resulting from the DMA selected size, as measured by the SMPS, and $dn/dr, dr$, are directly from the SMPS measurements. The integrals in the equation defining CE_{ch} effectively removes the large-particle contribution to $CE_{ch}(r_{mode})$. The equation could be simplified to the ratio of the OPC measurements minus the large particles above the channel boundary, to the CPC measurements minus the particles above the channel boundary, but this removes the explicit dependence on $CE_{Measured}$ and that the laboratory measurements must be normalized. Thus, the equation remains unsimplified.

Since $CEF_{ch}(r)$ is the desired CEF for the OPC channel nearest to r_{mode} and is to be derived from the counting efficiency measurements, the equation for $CE_{ch}(r_{mode})$ must be iterated. The a priori for CEF_{ch} is $CE_{Measured}$. The iteration uses CE_{ch} for CEF_{ch} until convergence, which occurs almost immediately. The

form of CEF_{ch} and its derivation is described in section 3.2 below. Due to the stable characteristics of the distribution of multiply charged particles in a DMA, the fraction of multiply charged particles is relatively constant. Thus, the multiply charged particle correction is most significant at particle sizes below an OPC channel where the counting efficiencies are small.

On 15 days from 2010 to 2012 and 1 day in 2018 counting efficiency laboratory tests were completed on five different OPC40s. The complete data set is shown in Figure 5. The counting efficiency measurements are plotted as a function of mode radii obtained from the SMPS analysis of the ammonium sulfate aerosol for each measurement. The radii used in Figure 5 are the ammonium sulfate radii converted to the equivalent size for sulfuric acid and water droplets, the aerosol for which the OPC40 is calibrated. Only three of the six instruments included an aerosol channel at 0.19 μm, hence the limited number of instruments contributing to Figure 5b. Managing the dilution system of filtered air to maintain relatively constant aerosol concentrations <10 cm^{-3} for a single 5-min measurement was a constant challenge, which increased for larger particles. Reliably generating particles larger than 0.3 μm at stable concentrations for the necessary time was beyond the capability of our DMA and experimental technique. Thus, the paucity of measurements above 0.3 μm in Figure 5d. Similar measurements were completed on the OPC25 and are shown in Figure 6.

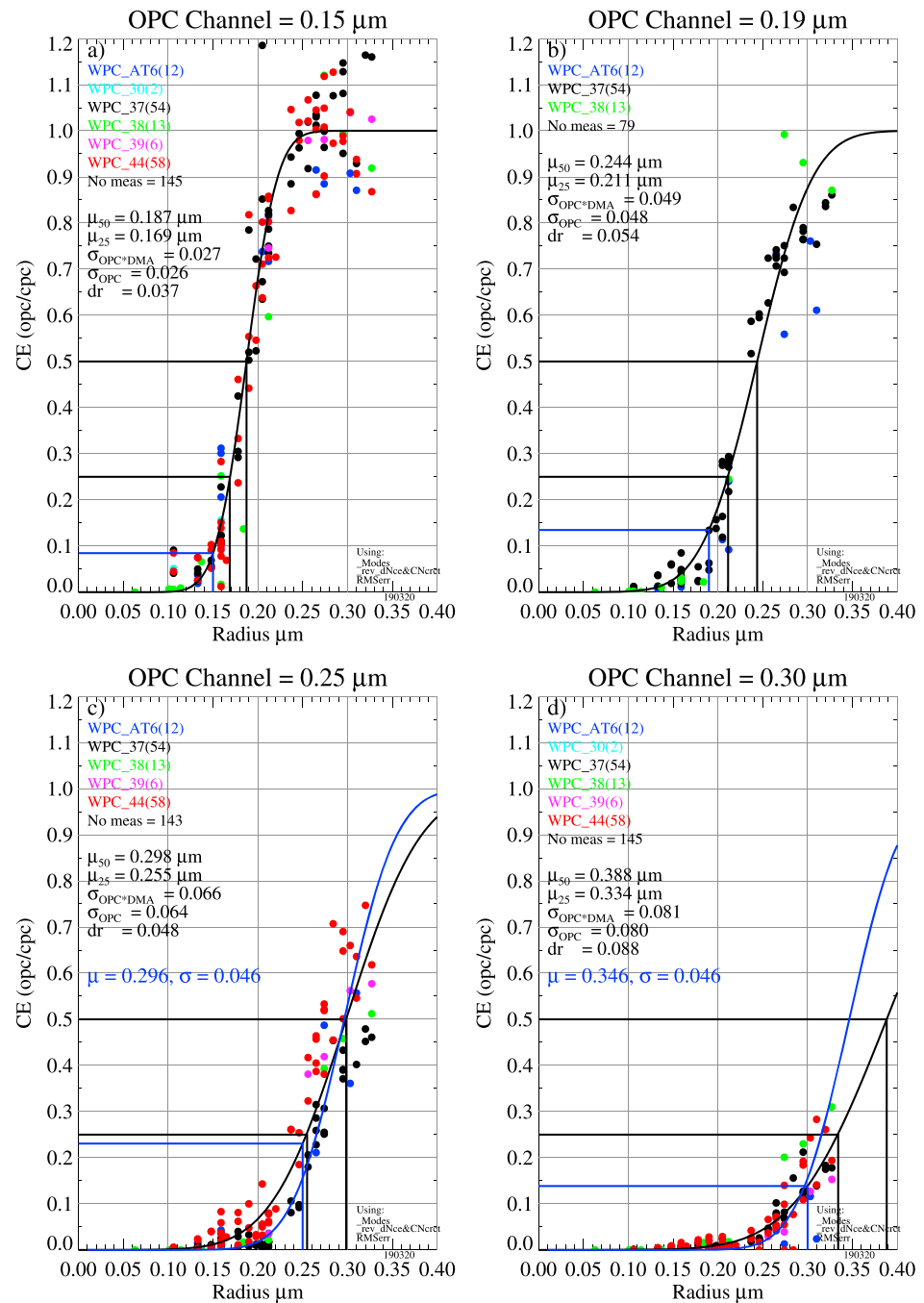Counting efficiency tests for OPC40 channels >0.3 μm are not possible due to the limitations of generating particles >0.4 μm at detectable concentrations using the DMA. Changing the aerosol to monodispersed PSL without using a DMA was also not a possibility. Although the OPC40 would only be sensitive to the PSL generated, a lot of small aerosol arise as residual material from evaporation of the hyper clean water used to aerosolize the PSL. These small aerosol would be sensed by the CPC; thus, there is no CPC reference concentration that is limited exclusively to the concentrations measured by the OPC40 at the larger aerosol sizes. It is reasonable to assume that the upper OPC40 channels behave the same as the lower channels, since the calibration procedures are the same.

3.2. Analysis of the Laboratory Counting Efficiency Measurements

The counting efficiency (CE) measurements in Figures 5 and 6 result from the convolution of three Gaussian distributions. The first Gaussian arises from the DMA generated sample aerosol, which, at each size measured, results from a narrow Gaussian distribution around the central size selected by the DMA, σ_{DMA} ranges from 0.001 to 0.005. Confirmation of this Gaussian is obtained from the SMPS measurements, not shown, for each PSL sample selected. The second and third Gaussians arise from the two PMTs used to obtain an OPC measurement. The output of each PMT is a Gaussian pulse height distribution, which arises from the pulse broadening inherent to the PMTs used in the instrument (Figures 1 and 2). While the distributions shown in Figures 1 and 2 are affected by small particle contaminants in the water, leading to questions about their Gaussian nature, PMT pulse height distributions created from a constant light source, used to characterize PMTs, display a clear Gaussian nature (Miao, 2001), as do monodispersed aerosol samples with contaminants removed (Pinnick et al., 1976) or monodispersed samples with concentrations exceeding the contaminants (Eidhammer, 2006). The PMT pulse height distributions have been used to assess the precision of the OPC40 measurements of particle size. The OPC only counts particles which produce voltage pulses above the comparator level from both PMTs. Thus, the two PMT Gaussian distributions are already convolved into the OPC measurement. Although the PMT distributions in Figures 1 and 2 are shown in voltage space, they could also be represented as distributions in radius space using the CRF.

The convolution of Gaussian distributions is also a Gaussian distribution with well-defined dependencies between the convolved distribution and the underlying distributions (Hirschman & Widder, 1955; Morse & Feshbach, 1953). Thus, it is reasonable to use a Gaussian function to represent the CE data shown in Figures 5 and 6 since they result from the convolution of three Gaussian distributions. The measured counting efficiency of any OPC channel can be represented as the integral of a Gaussian distribution, or cumulative distribution function, characterized by a distribution median, μ, and width, σ. The counting efficiency of the OPC for any channel, CEF_{ch}, can then be represented for any particle size as follows:

$$CEF_{ch}(r) = \frac{1}{2}\left[1 + \text{erf}\left(\frac{r-\mu}{\sqrt{2}\ \sigma}\right)\right], \text{where} \quad \text{erf}(z) = 1/\int_{-z}^{z} \exp\left(-t^2\right)\,dt. \quad (1)$$

Figure 5. Laboratory measured OPC40 counting efficiencies (CE = opc/cpc) at OPC40 channels of (a) 0.15, (b) 0.19, (c) 0.25, and (d) 0.30 μm using up to six different OPC40s. The tests were conducted on 15 different days over 3 years. The cumulative distribution functions (CDFs) derived from the measurements at each OPC40 channel size are shown as the black curves. The gray vertical and horizontal lines indicate μ_{50} and μ_{25}, which are listed at the top along with $\sigma_{OPC*DMA}$, σ_{OPC}, and dr for each CDF. The counting efficiency of the nominal channel size is shown with the blue vertical and horizontal lines. In (d) the CDF in blue with μ and σ shown in blue is the average dr and σ from the first three OPC40 channels. OPC = optical particle counter; DMA = differential mobility analyzer.

The characteristics of CEF_{ch} are that it is ~0 for $r \ll \mu$, 0.5 for $r = \mu$, and 1 for $r \gg \mu$. Thus, μ becomes the radius representing the 50% counting efficiency point for any one channel of the instrument, thus μ_{50}. CEF_{ch} has the right limiting behavior, and the rate at which CEF_{ch} approaches the lower and upper limits, 0 and 1, is determined by σ.
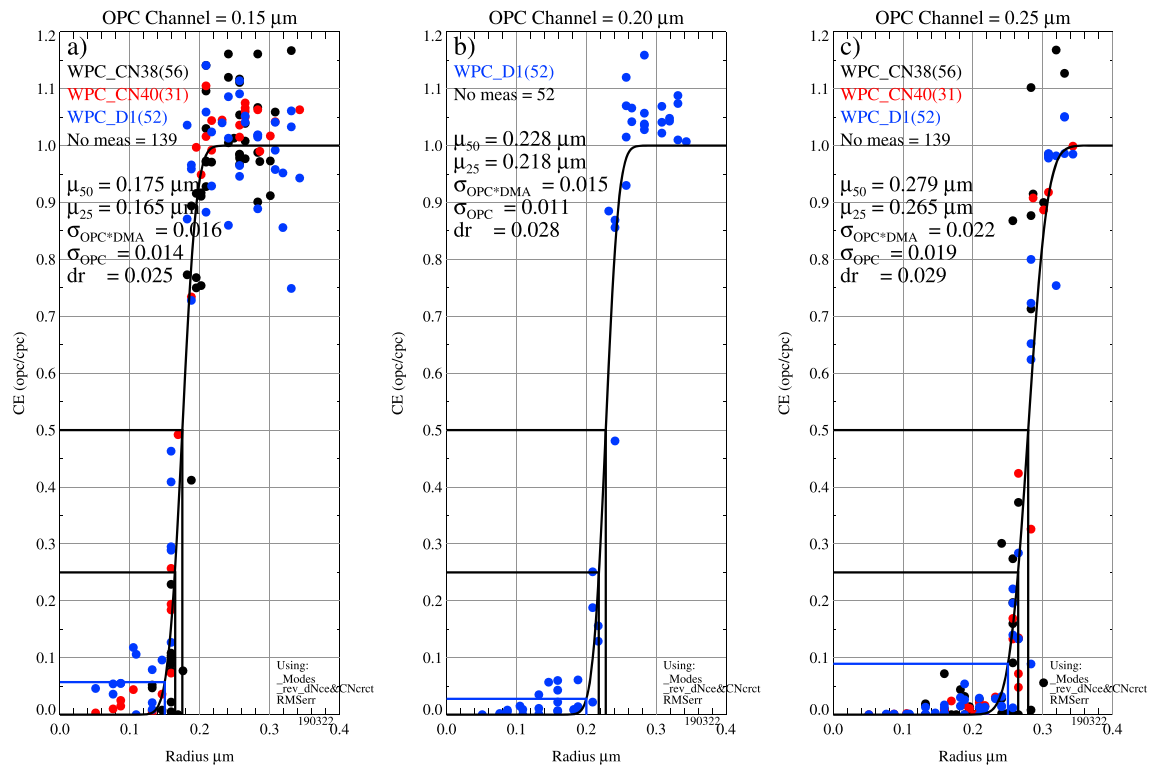
Figure 6. Same as Figure 5 except for OPC25 channels of (a) 0.15, (b) 0.20, and (c) 0.25 μm.

A least squares method was used to derive μ_{50} (ch) and σ (ch), which provided a CEF_{ch} best representing the counting efficiency measurements for the OPC channels shown in Figures 5 and 6. The solid black curves in each panel represent CEF_{ch} with μ_{50} and σ shown, along with μ_{25}, the particle radius which produces a 25% counting efficiency, and $dr_{ch} = \mu_{50}(ch) - r_{ch}$, where r_{ch} is the nominal OPC channel size, which was the target calibration size. Thus, dr_{ch} is the shift in the 50% counting efficiency point between the target calibration boundary, r_{ch}, and the channel boundary derived using the Gaussian fit to the data, μ_{50}. Considering the way the OPC40s were calibrated, μ_{25} should approximate the calibration target OPC40 channel boundaries, and, within 0.01–0.02 μm, this is the case for the first three OPC40 channels. In contrast for the OPC40, dr_{1-3} of the fitted CEFs ranged from 0.037 to 0.054 μm, which is an indication of the error, which affects the previously reported measurements (Deshler et al., 2003).

There are a few points at 0.11 μm in Figure 5a, which are significantly underestimated by the black CEF curve. This could be important since a curve which passes closer to these points would have an impact, particularly on the SAD derived from the measurements. While Figure 5a suggests there are four points, two from WPC_37 and two from WPC_44, in fact the overlapping points are dependent. The measurements were completed by both instruments at the same time for each of the pair of points, so realistically there are only two independent measurements. If there were any experimental difficulties, such as a minor leak in the plumbing leading to the instruments, it would affect both measurements similarly. It is reassuring that both OPC40s reproduced each other for these two points. Given the importance of these points, four additional CEF measurements were made in April 2018 using WPC_38, the last working OPC40, at sizes between 0.06 and 0.16 μm, including several measurements near 0.11 μm. These appear as the green data points and lie right on the CEF curve at 0.11 μm, further casting doubt on the several points between a CE of 0.04 and 0.08 at 0.11 μm in Figure 5a.

The σ derived from the CE data results from the convolution of two Gaussians, one from the DMA and one from the OPC, hence $\sigma_{OPC * DMA}$, whereas the σ to use to characterize the OPC $CEF_{ch}(\mu, \sigma)$ should not include σ_{DMA}. An investigation of the SMPS data for all the CE measurements led to a fairly robust distribution of σ_{DMA} versus r_{mode} with values of $\sigma_{DMA} \sim 0.01$. Determining the distribution width of a

Table 1
Parameters Used to Derive the CEFs Shown in Figures 5 and 6 for the OPC40 and OPC25

r_{ch} (μm)	μ_{25}	μ_{50}	σ_{OPC}	$\mu_{50} - r_{ch}$
OPC40				
0.15	0.169	0.187	0.026	0.037
0.19	0.211	0.244	0.048	0.054
0.25	0.255	0.298	0.064 (0.046)	0.048 (0.046)
≥0.3	0.334	r_i + 0.046	0.046	0.046
OPC25				
0.15	0.165	0.175	0.014	0.025
0.19	0.218	0.228	0.011	0.028
0.25	0.265	0.279	0.019	0.029

Note. The numbers in parentheses in the 0.25 μm row indicate the numbers used in the size distribution retrievals. CEF = counting efficiency function; OPC = optical particle counter.

single Gaussian from a convolution of two Gaussians is given by $\sigma_{OPC} = \sqrt{\sigma_{OPC*DMA}^2 - \sigma_{DMA}^2}$. This result was used to derive a final σ_{OPC} for each OPC40 channel. The parameters, r_{ch}, μ_{25}, μ_{50}, σ_{OPC}, and dr_{ch} are listed in Table 1 for OPC channels 1–3. For OPC channel 3 and larger, assumptions for μ_{50} and σ_{OPC} are required.

The measurements for the 0.25- and 0.3-μm channels are insufficient to characterize the performance of the instrument in regions where the counting efficiency should be near one. This impacts the fitted estimates of μ_{50} and σ_{OPC} for the 0.25- and 0.30-μm channels. For these channels, and all larger channels, μ_{50} and σ_{OPC} are estimated from $\mu_{50} = r_{ch} + <dr_{1-3}>$ and $\sigma_{OPC} = <\sigma_{OPC}(1-3)>$, where $<x>$ implies the mean of x. The blue curves in Figures 5c and 5d use these approximations for μ_{50} and σ_{OPC}. Given the paucity of measurements in the regions where the CEF should be near one for the 0.25- and 0.30-μm channels, the only empirical choice is to rely on averages of the measurements in the first three channels to provide estimates for dr and σ_{OPC} for all channels≥0.25 μm. These assumptions give the CEF illustrated with the blue curves in Figures 5c and 5d and are listed in Table 1. Fortuitously, to three decimal places, the values of $<dr_{1-3}>$ and $<\sigma_{OPC}(1-3)>$ are both 0.046.

From Table 1 the counting efficiency of the first three channels of the OPC40s at the nominally calibrated sizes of 0.15, 0.19, and 0.25 are near $\mu_{25}(ch)$. This was expected based on the analysis of the coincidence counting discussed above and as used by KD15. For OPC25, $dr_{ch} = \mu_{50} - r_{ch}$ is about half to two thirds of that obtained from the OPC40 measurements, and $\mu_{50}(ch)$ is closer to r_{ch} as expected from the alternate calibration system for these instruments. The OPC25 distributions are significantly narrower than the OPC40 distributions, indicating much more well defined cut points.

3.3. Impact of the Counting Efficiency Results on Wyoming OPC In Situ Measurements

The fundamental measurement for any OPC is a number concentration in each channel based on the number of pulses counted. The counting efficiency tests just described do not impact the OPC number concentrations; rather, they impact the sizes associated with any one OPC channel. Accepting this result brings the approach here into a fundamental difference with the approach of KD15 to correct for the OPC40 calibration error. KD15 used the CE tests to confirm the calibration error and then corrected the OPC number concentration to reflect the aerosol number concentration at the nominal OPC channel sizes. Here we assume that the unknown in the measurement is the channel size, which is dependent on instrument design, calibration, and laboratory testing. The results from the laboratory counting efficiency measurements are used to adjust the channel sizes reported for the Wyoming in situ measurements made using either the OPC40 or OPC25 but leaves the fundamental measurement, the number concentration, undisturbed.

This new approach impacts the measurements from 1971 to 1991 for the OPC25 and 1991 to 2012 for the OPC40. The new channel sizes are defined by $\mu_{50}(ch)$ and will be reflected in the column labels for the aerosol concentration data from the instruments. The data with the corrected sizes will be in the folders under …/UWv2.0/ on the publicly available web site. These changes also impact the size distributions derived from the data and, when the full counting efficiency curves are taken into consideration, induce some complications into the derivation of the size distributions, which previously was relatively straightforward.

4. Retrieval of Aerosol Size Distributions From Wyoming OPC Measurements

Using aerosol data in climate chemistry models or comparing aerosol measurements across instruments almost always requires obtaining a moment of the aerosol size distribution, either aerosol surface area, cross section, volume, or extinction. These moments can be obtained by summing in situ size distribution measurements (a Riemann sum), if the size channels have a resolution high enough to capture fine-scale variations and extend to sizes which cover the natural aerosol size distribution. Almost all OPC measurements have limitations below 0.1 μm such that the aerosol size distribution from 0.01 to 0.1 μm is poorly measured.

To circumvent these problems and still satisfy the need for distribution moments, lognormal size distributions are often fit to aerosol measurements (Hofmann & Deshler, 1991; Jäger & Hofmann, 1991; Pueschel et al., 1992, 1994). The lognormal size distributions may be unimodal or multimodal depending on the number of size channels available and on the characteristics of the natural aerosol size distribution. Each mode of a lognormal size distribution requires three measurements. These measurements can be the total number concentration and the number concentration at two sizes or the number concentration at three sizes. For the Wyoming OPC measurements the OPC25/OPC40 instruments were almost always accompanied by a condensation nuclei (CN) counter to provide the total aerosol population (Campbell & Deshler, 2014; Rosen et al., 1978), which was used in fitting size distributions to the OPC measurements. Since the OPC25 typically only made measurements at two sizes, unimodal lognormal distributions are used to represent these measurements. Even when aerosol channels were added at 0.2 and 0.3 μm, they seldom provided enough additional information to justify a second mode, since they were not significantly different than the standard aerosol channels at 0.15 and 0.25 μm. The size limitations of this instrument suggest that size distributions derived during periods of heavy aerosol loading, such as after large volcanic eruptions, are probably misleading in missing a second large-particle mode. These concerns led to the development of a 50 L/min OPC flown following Mt. St. Helens and El Chichón, 1982–1986 (Hofmann & Rosen, 1982).

Rosen and Hofmann (1986) and Deshler et al. (2003) describe different approaches for deriving aerosol size distributions to OPC data when measurements at sizes >0.3 μm are available. Rosen and Hofmann used a lognormal distribution to describe the small-particle measurements and a spline function at the larger sizes, obtained from the 50-L/min instrument, which is a nonstandard distribution and requires parameters, which do not have a clear physical significance. The advantages of using multimodal lognormal distributions are that three parameters describe each mode of the distribution; each of these has a physical significance, total number concentration in the mode, median radius, and distribution width; the lognormal distributions usually represent the data well; and there are analytical expressions for the distribution moments. Finally, there is some reason to expect that aerosol concentrations naturally evolve to lognormal distributions (*Granqvist & Buhrman,* 1976), for aged aerosol such as stratospheric aerosol.

4.1. Size Distribution Retrieval Not Accounting for Aerosol Counting Efficiency

The algorithm developed by Deshler et al. (2003) to fit unimodal/bimodal lognormal size distributions to the OPC number concentration measurements, N_{ch}, assumes the data can be represented with a unimodal/bimodal lognormal size distribution (equation (2)).

$$N_{ch} = \int_{r_{ch}}^{\infty} \left[\sum_j \mathrm{d}n_j / \mathrm{d}\ln[a] \right] \mathrm{d}\ln(a) = \int_{r_{ch}}^{\infty} \left[\sum_j \frac{N_j}{\sqrt{2\pi} \cdot \ln[\sigma_j]} \exp\left[\frac{-\ln^2[a/\mu_j]}{2 \cdot \ln^2[\sigma_j]} \right] \right] \mathrm{d}\ln(a) \qquad (2)$$

where the summation, j, is over either one or two modes of the size distribution. For each mode of the distribution, N_j is total number concentration in the mode, μ_j median radius, and σ_j distribution width. N_{ch} represents the concentration of all particles larger than the lower integration limit, r_{ch}, and is assumed to be the quantity measured by the OPCs for each OPC channel, ch. The total number concentration, or CN concentration, is obtained when the lower integration limit is set to some low value, say, 0.01 μm. $N(r>0.01 \text{ μm}) = N_1 + N_2$ = the CN concentration, which is measured. Note that the median radius, μ_j, and distribution width, σ_j, are different variables than the variables μ_{50} and σ_{OPC} used above for describing CEF_{ch}.

The fitting method consists of minimizing the root-mean-square (RMS) error = $\sqrt{\sum_{ch} \log^2[N_{ch}(m)/N_{ch}(Eq2)]}$. The summation, ch, is over all measured sizes, r_{ch}. $N_{ch}(m)$ is the measured concentration for all particles with $r > r_{ch}$, N_{ch} (Eq (2)) is defined by equation (2). The method for a unimodal distribution consists of trying all pairwise combinations of measured concentrations at specific OPC sizes to find the two OPC sizes, plus CN concentration, giving unimodal size distribution parameters, which minimize the RMS error when the calculated number concentrations are compared to the measured number concentrations at all sizes. This RMS error is stored for comparison to the bimodal distribution.

Fitting bimodal distributions requires first identifying the size, or break point, r_{bp}, to separate the two lognormal distributions. For each possible r_{bp} between r_2 and r_{nr-2}, for nr measurements, the measurement space is searched pairwise across sizes, $r_i < r_{bp}$ and $r_j > r_{bp}$, for r_{bp} and the two subsets of three measurements: $[N_1, N(r \geq r_i), N(r \geq r_{bp})]$, $[N_2, N(r \geq r_j), N(r \geq r_{nr})]$, which minimize the RMS error when the modeled distribution is compared to the measurements at each OPC size. The third element in each measurement subset is fixed to the largest size in that set to insure the tail of the distribution is well constrained. Further $N(r \geq r_{bp})$ is artificially lowered to insure the second mode concentrations do not influence the first mode fit. The a prioris for N_1 and N_2 are $CN - N(r \geq r_{bp})$ and $N(r \geq r_{bp})$, but these change as does $N(r \geq r_j)$ as the optimization searches for the best lognormal fits. Then N_2 is defined as $CN - N_1$, where N_1 is the integral of the first mode of the size distribution and $N(r \geq r_j)$ is adjusted to remove any number concentration contribution from the first mode. The RMS errors from comparing the measurements to the bimodal and unimodal lognormal distributions are then compared and the best fit chosen. The fitted size distributions are not forced to be bimodal. If a unimodal distribution provides a better fit then that is used, but this is seldom the case when there are more than four independent measurements.

To obtain bimodal distributions requires a minimum of five independent measurements of number concentration. If necessary, the sixth measurement is obtained by setting the concentration, at the first size in which there are no counts, to a value below the detection limit of the instrument, $\sim 10^{-4}$ cm^{-3} for an OPC40. If there are less than five independent concentration measurements, then a unimodal distribution is applied. This is the case for all OPC25 measurements unless they were supplemented with the 50 L/min counter mentioned earlier.

Uncertainties of the aerosol moments and size distribution parameters were assessed by Deshler et al. (2003) using a Monte Carlo simulation of the fitting algorithm, where the input data for each fit was randomly altered based on uncertainties in aerosol concentration and aerosol size. The uncertainties in aerosol concentration arise from Poisson counting statistics and precision, while the uncertainties in aerosol size arise primarily from pulse width broadening with a range of 10–30%. The results were uncertainties of $\pm 40\%$ for moments of the aerosol size distribution, $\pm 30\%$ for median radii, and $\pm 20\%$ for distribution width. Considering that all of the uncertainties included in Deshler et al. (2003) still apply to the measurements, even though the channel sizes and fitting method have changed based on the work described here, the same uncertainties are still expected to apply to the OPC measurements.

4.2. Size Distribution Retrieval Including Aerosol Counting Efficiency

To account for the counting efficiency at each aerosol channel requires modifying equation (2) by including $CEF_{ch}(a)$ explicitly in the expression representing the OPC measurement at each channel, N_{ch}. Thus,

$$N_{ch} = \int_0^\infty \left[\sum_j dn_j / d\ln(a) \right] CEF_{ch}(a) \, d\ln(a). \tag{3}$$

Now the integration is over all possible sizes since $CEF_{ch}(a)$ will approach zero for particles much below the median radius of the aerosol channel, $a \ll \mu_{50}(ch)$, and will approach one for $a \gg \mu_{50}(ch)$. In the region between these limits $CEF_{ch}(a)$ will provide a realistic assessment of how well the OPC counts particles near the nominal aerosol channel r_{ch}, which ideally is $\mu_{50}(ch)$. The extent of the region around $\mu_{50}(ch)$ where $0 < CEF_{ch}(a) < 1$ is controlled by the width, $\sigma_{OPC}(ch)$ of CEF_{ch}. Previously, when the counting efficiency was ignored, the calculation of a measurement only required integrating the aerosol distribution function $dn/d\ln(a)$ from $\mu_{50}(ch)$ to infinity. Implicit in equation (2), but not previously acknowledged, is a hidden CEF, with $\sigma_{OPC} = 0$, implying $CEF(a < \mu_{50}(ch)) = 0$ and $CEF(a \geq \mu_{50}(ch)) = 1$. The form of the size distribution in square brackets in equation (3) is arbitrary, although for application to the OPC data these are assumed to be given by the lognormal distribution in the integrand in the right hand side of equation (2). Also implicit in equation 2 is the assumption that the nominal OPC40 calibration sizes, which are reported for each OPC40 channel, represent $\mu_{50}(ch)$. It is clear from Figures 5 and 6 that the previously reported $\mu_{50}(ch)$ have to be modified as indicated above and in Table 1. Thus, each CEF_{ch} is defined by a $\mu_{50}(ch)$ and $\sigma_{OPC}(ch)$, which result from the laboratory measurements for the smaller channels and extrapolations of these results for the larger channels.

The size distribution fitting method previously employed for the Wyoming in situ data (*Deshler* et al., 2003; *Hofmann & Deshler,* 1991; *Jäger & Hofmann,* 1991), all used equation (2). This allowed a subset of the measurements to determine the lognormal parameters for any mode of the distribution, the straightforward pairwise searches of the measurements described above for the unimodal/bimodal lognormal parameters. When, instead, the laboratory counting efficiency and equation (3) are used, that method will not work. A concentration measurement is no longer tied explicitly to all particles larger than just one particle size; rather, the measurement at any one channel is influenced by the counting efficiency for particles surrounding the channel boundary, defined by the CEF_{ch}. The previous lognormal fitting method has to be abandoned.

The general approach of minimizing the RMS error when the measurements are compared to the fitted size distributions at the measurement sizes is retained but with two major changes. Calculating the measured concentration at any one channel, N_{ch}, from a candidate size distribution is completed using equation (3), where the candidate size distribution, $dn/dln(a)$, is a unimodal/bimodal lognormal size distribution as defined in equation (2). Because each measurement can no longer be associated with a specific size, searching for the best size distribution parameters using the measurements directly is not possible. Rather, for each aerosol concentration measurement a search of the parameter space for the median radius, μ, and distribution width, σ, of a lognormal distribution to fit the data, must be performed. Recall that the symbols μ and σ represent the median and distribution width for a lognormal size distribution not a CEF, for which μ_{50} and σ_{OPC} are used. For a bimodal distribution, before beginning this search, it is necessary to determine the break point between the two distributions and hence N_2, the concentration at the break point size. This is done using the old method and the data directly. Searching a large parameter space for N_2 for each of the candidate channels to represent the break point is not practical, nor as the results will show, necessary. Once N_2 is determined, N_1 is determined as before. For a unimodal distribution N_1 is defined as the CN concentration.

The searches for the lognormal parameters, μ and σ, are done systematically for each mode of the distribution using the range: $\mu = 0.02 - r_{n-1}$, where r_n is the radius of the largest of the n aerosol channels measured and $\sigma = 1.03–3.5$. The entire range of one parameter is searched for each element of the range of the other parameter. The RMS error is calculated for each pair, μ_i, σ_i, for each size distribution mode. The RMS error is well behaved without multiple minimums. Two passes through the parameter space are used to increase the resolution used for μ and σ by decreasing the grid spacing around the coarse grid defined RMS minimum. Before the random search is begun for any OPC40 measurement, the nominal aerosol size for each channel, $\mu_{50}(ch)$, is adjusted for evaporation in the inlet using the method described by KD15, which is ambient temperature and pressure dependent. Thus, this is done for each measurement altitude.

As a test of the parameter space search method for obtaining lognormal fitting parameters, this method was compared to the explicit pairwise search method of Deshler et al. (2003), assuming for both methods that the measurements can be described with equation (2). The results agreed well justifying the robustness of the two techniques. However, when the explicit CEF is included, equation (3), there are systematic differences in the lognormal parameters as expected. Differences between the explicit CEF method and the pairwise search method without a CEF (*Deshler* et al., 2003) are shown in Figure 7. The differences are primarily apparent in the first mode of the size distributions (Figures 7a for a volcanic case, mode radius triples, and Figure 7b for a nonvolcanic case, mode radius increases bv 50%). In both cases the distribution widths decrease. For the second mode of the distribution there is little change for both cases. Overall, differences in the distribution moments are shown in Figures 7c for a volcanic case and Figure 7d for a nonvolcanic case. There is a clear systematic increase in both SAD and volume density, with the increase more significant in the nonvolcanic case for the explicit CEF fits compared to Deshler et al. (2003). Differences between altitude integrals of SAD and volume and averages of differences at each altitude, $Fn(z)$, are 30–80% for the volcanic case and near 200% for the nonvolcanic case. These figures are typical of many such comparisons.

While bimodal lognormal fits to the OPC40 data generally reproduce the measurements quite well as shown in Figure 7, the data gap between the total aerosol concentration, nominally taken to be all particles >0.01 μm, and the first size resolved channel at 0.15 μm should not be glossed over. How this region is fitted can have significant impacts on distribution moments, particularly SAD during nonvolcanic periods. As a test of the importance of the CEF parameters for the 0.15-μm channel, which impacts the fitting between 0.15 and 0.01 μm, the distribution width, σ_{OPC}, for the 0.15-μm channel was artificially increased to 0.048
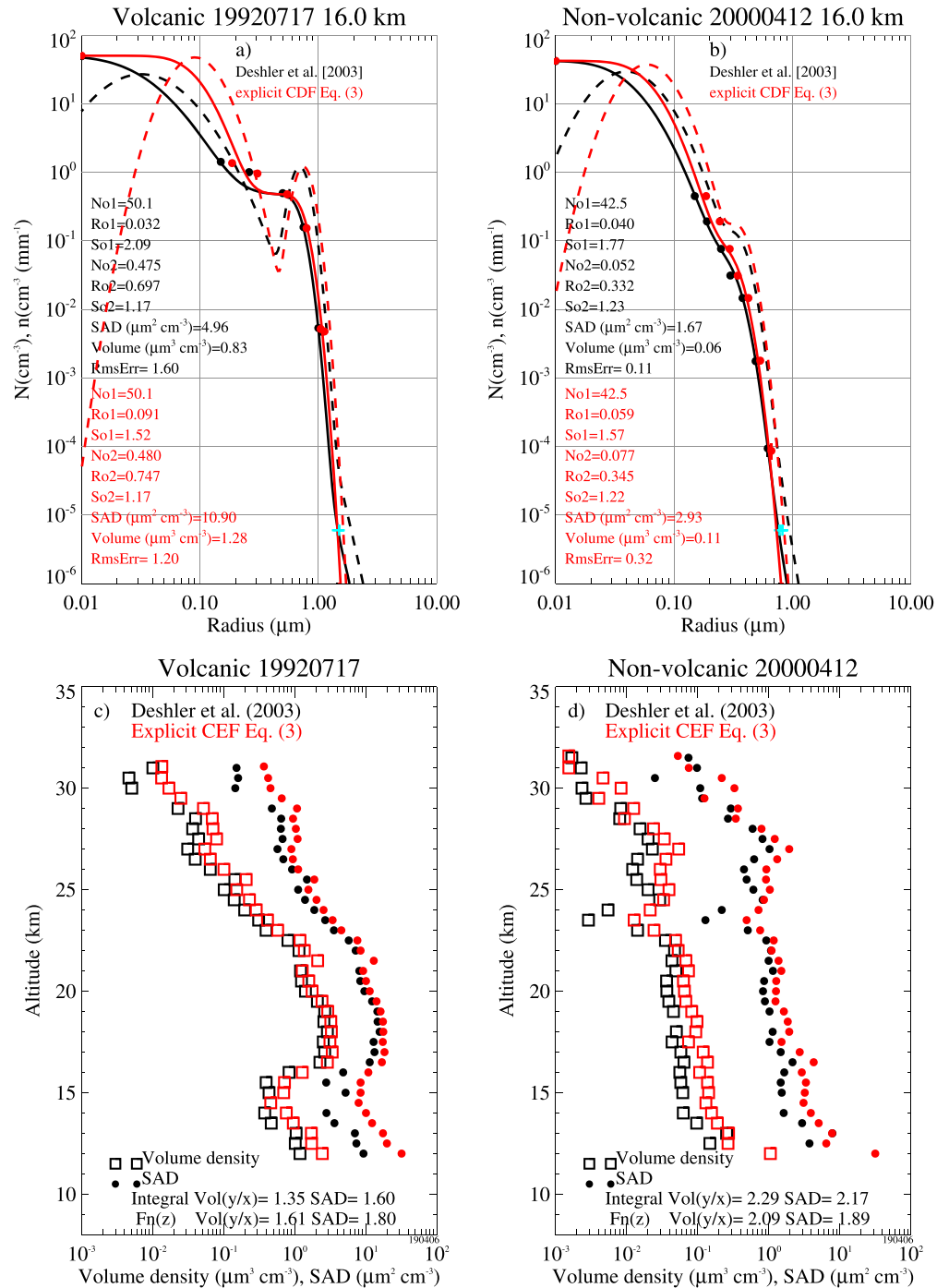
Figure 7. (a, b) Cumulative (solid) and differential (dashed) size distributions compared to measurements (dots) at 16 km for (a) 17 July 1992 in the volcanic period and (b) for 12 April 2000 in the nonvolcanic period. Size distributions and data points are shown for the original OPC40 data and the Deshler et al. (2003) fits (black) and for the retrievals using an explicit counting efficiency function (red). Lognormal parameters for the fits are listed in the figures along with surface area density (SAD) and volume density. (c, d) Profiles of volume density (squares) and SAD (filled circles) derived from Deshler et al. (2003) (black) and from explicit counting efficiency functions (red) for (c) 17 July 1992 and (d) 12 April 2000.

as an extreme difference. The impacts on SAD compared to the value of $\sigma_{OPC} = 0.026$, Figure 5, indicated a decrease in SAD in the nonvolcanic period ranging from 50% to 100% with the artificial value of σ_{OPC}. Other distributions with different break points between the two modes have also been tried, can fairly represent the measured size distributions, and lead to similar changes in SAD, although such distributions do not arise from the optimum search method employed here. There is little in the OPC40 data to clarify how to handle the gap between 0.15 and 0.01 μm. Such clarification requires comparisons of the derived size distributions with independent measurements of stratospheric aerosol.

5. Comparison of In Situ and Remote Satellite Measurements

Measurements of stratospheric aerosol are provided by satellite remote sensors, lidar, and balloon- and aircraft-borne in situ particle counters. The satellites provide global coverage; the ground- and airborne-based instruments provide more highly resolved vertical profiles at limited locations. With the global coverage from the satellite instruments comparisons can be made against single lidar locations (Khaykin et al., 2017), against aircraft in situ measurements in the lower stratosphere (Reeves et al., 2008) and against balloon-borne in situ measurements (Thomason et al., 1997; KD15). The opportunities for comparisons between lidar and in situ measurements are more limited and somewhat confined to the polar regions (Adriani et al., 1995; Deshler et al., 2000). Coordinating a comparison between aircraft and balloon measurements has proven challenging (Borrmann et al., 2000, 2010). Thus, the bulk of the comparisons between the Wyoming in situ data and other measurements have been with various satellite instruments (Lambert et al., 1996; Hervig et al., 1996; Thomason et al., 1997; KD15).

5.1. Deriving Aerosol Extinction From Aerosol Size Distributions

For comparisons of the in situ data with remote sensors requires using the in situ aerosol size distributions to derive aerosol extinction or backscatter. These are accomplished with the following equation.

$$\beta_\lambda(m) = \int\limits_0^\infty \pi a^2 \cdot Q(a, \lambda, m) \cdot dn/d\ln(a) \cdot d\ln(a), \qquad (4)$$

where β is either extinction or backscatter at wavelength λ for particle index of refraction, m, Q is the extinction or backscatter efficiency, and $dn/d\ln(a)$ is the aerosol size distribution in the form given above by equation (2), with the size distribution parameters, μ_j, σ_j, derived using either equation (2) or (3). Following KD15 the comparisons to be shown here will be made with SAGE II and HALOE measurements of aerosol extinction within reasonable geographic correspondence with Laramie and times of the in situ measurements.

As equation (4) indicates, β_λ is dependent on the index of refraction through the extinction efficiency, $Q(r, \lambda, m)$, which is a function of particle composition. Stratospheric aerosol are primarily small droplets of sulfuric acid and water (Arnold et al., 1998; Murphy et al., 1998; Rosen, 1971), with the composition typically given in weight percentage (wt %) of H_2SO_4. The weight percent of the acid is dependent on temperature and water vapor concentration. For the time period of these calculations a stratospheric water vapor concentration of 4.5 ppmv appears to be a reasonable approximation over the 15- to 30-km altitude range above Laramie (Hurst et al., 2011). Dependent upon temperature, calculated extinctions vary from 1% to 5%, averaging 2% over a profile, for water vapor concentration in the range of 4–6 ppmv. Steele and Hamill (1981) provide a relationship between temperature and weight percentage of sulfuric acid. This relationship was fit with an analytical expression by Hanson et al. (1994) to determine the weight percent as a function of temperature and water vapor concentration. Palmer and Williams (1975) provide sulfuric acid and water refractive indices at 300 K over the wavelength range from 0.37 to 7.2 μm for specific weight percentages in the range of 25–95%. By interpolation, indices of refraction can be determined for any acid concentration and wavelength within these ranges. Finally, the real part of the refractive index, $m(T)$, is corrected to the measured stratospheric temperature, T, using the Lorentz-Lorenz formula:

$$m(T) = \sqrt{\left(\frac{1 + 2A\rho(T)}{1 - A\rho(T)}\right)}, \quad \text{where} \;\; A = \frac{m^2(300) - 1}{[m^2(300) + 2]\rho(300)}. \qquad (5)$$

The density of sulfuric acid, $\rho(T)$, is calculated from Luo et al. (1996), $m(300)$ is the index of refraction from Palmer and Williams (1975).

Table 2
Number of Comparison Profiles Between OPC40 and SAGE II and Between OPC40 and HALOE

Instrument	Volcanic		Nonvolcanic	
	This paper	KD15	This paper	KD15
SAGE II	67	80	29	22
OPC40	31	34	19	12
HALOE	65	75	13	14
OPC40	27	31	5	5

Note. The comparisons used are labelled as "this paper" and the ones used in Kovilakam and Deshler (2015) as "KD15." OPC = optical particle counter; SAGE = Stratospheric Aerosol and Gas Experiment; HALOE = Halogen Occultation Experiment.

For SAGE II wavelengths the refractive index has only a real (scattering) component, whereas for HALOE there is also an imaginary (absorbing) component for wavelengths >2.5 μm. As for SAGE II, the refractive indices for HALOE are from Palmer and Williams (1975). At HALOE wavelengths there is little dependence of index of refraction on weight percent between 60% and 80%; thus, no adjustments are made for stratospheric temperatures. The refractive indices from Palmer and Williams at 300 K are used. Given the refractive index, Mie theory for spherical particles is used to calculate extinction efficiency as a function of particle radius for SAGE II and HALOE. The results of the extinction efficiency calculations for SAGE II and HALOE wavelengths are shown in Figure 6 of KD15 and not repeated here.

5.2. SAGE II and HALOE Measurements and Coincidence Criteria

SAGE II was launched on the Earth Radiation Budget Satellite on 5 October 1984. The SAGE II spectral radiometer measures solar occultation at seven wavelengths during approximately 15 sunrises and sunsets per day (Mauldin et al., 1985). Solar transmission through the Earth's limb during sunrise/sunset is then used to derive aerosol extinction and the concentrations of ozone, nitrogen dioxide, and water vapor (Chu et al., 1989; Damadeo et al., 2013; Wang et al., 1994). Measurements are taken from a tangent height of 150 km, where there is no attenuation, down to where the Sun is obscured by clouds or terrain. The vertical resolution is 0.5 km with a spatial coverage from 80°N to 80°S. SAGE II aerosol extinction measurements are reported at 0.386-, 0.452-, 0.525-, and 1.02-μm wavelengths. The SAGE II version 7.0 data product is used here (Damadeo et al., 2013). Changes in the version 7.0 data include corrections to the solar ephemeris processing, updated ozone and nitrogen dioxide cross sections, other changes to the spectroscopy, and modifications to the transmission processing and inversion algorithms. Aerosol extinction was primarily affected by the changes in spectroscopy. These led to significant increases, 20–35%, in aerosol extinction at 0.525 and 0.452 μm, but minimal changes at 1.02 μm (Damadeo et al., 2013).

HALOE, launched on the upper atmosphere research satellite, provided science measurements from 11 October 1991 to 21 November 2005. HALOE, also a solar occultation instrument, measured profiles of seven gases (hydrochloric acid, hydrogen fluoride, methane, nitric oxide, nitrogen dioxide, water vapor, and ozone), temperature, and aerosol extinction at four wavelengths (2.45, 3.40, 3.46, and 5.26 μm; Russell et al., 1993). Latitudinal coverage is from 80°S to 80°N, and the altitude range extends from about 15 to 60–130 km depending on the species.

The data sets selected from SAGE II and HALOE, for comparison with the new retrieval of the OPC40 measurements, follow the same criteria as used by KD15. The data are separated into a volcanic, following the eruption of Pinatubo, and a nonvolcanic period. The coincidence criteria for measurements near Laramie, Wyoming (41°N, 105°W), for both periods are the same. Coincident measurements are identified using a maximum separation of 168 hr from the time of a balloon flight, a 6° latitude band centered at Laramie, and longitudes between 90°W and 120°W. The rationale for the widths of the latitude/longitude windows is that in the midlatitude midstratosphere the aerosol are primarily zonally homogeneous, allowing a wide longitude window. The time window was necessary to obtain a reasonable number of coincidences for the satellite comparisons. The balloon flights always occur early in the morning and are quite infrequent compared to the satellite measurements. While more appropriate coordinates to bracket the comparisons, such as potential vorticity and potential temperature, could be used, considering the wide sampling windows employed, the results are not expected to be very dependent on fine tuning individual comparisons. In addition, the comparisons to be shown here will be compared to KD15; thus, it is appropriate to use the same comparison criteria as KD15. The number of satellite and OPC40 profiles compared during each period and for each satellite is listed in Table 2 for the analysis here and for that by KD15.

For the OPC40 profiles in the volcanic period there are three fewer SAGE II comparisons and four fewer HALOE comparisons here than used by KD15. This is due to the removal of five flights in 1994, which had an inlet heated to 160 °C on ascent as part of another study at that time. In contrast, the number of OPC40 profiles in comparison with SAGE II in the nonvolcanic period has increased by seven profiles.

Five of these profiles were added from measurements prior to the Pinatubo eruption, and two additional OPC coincidences were found, one in 1997 and one in 1999. The five profiles prior to Pinatubo were added when it was discovered that KD15 had mistakenly included, in the averaged SAGE II volcanic profile, measurements between January and July 1991. These five OPC40 measurements prior to Pinatubo led to seven SAGE II profiles moved from the volcanic comparison to the nonvolcanic comparison. The other six SAGE II profiles removed from the volcanic comparison were those associated with the five heated inlet OPC40 profiles in 1994, as were the 10 HALOE profiles subtracted from the volcanic comparison. The one HALOE profile removed from the nonvolcanic comparison was one that had too large a separation from the OPC40 measurements.

5.3. Comparisons of SAGE II and HALOE Measurements With In Situ Derivations of Aerosol Extinction

For comparisons with the satellite measurements of aerosol extinction, four derivations of aerosol extinctions from the in situ data are provided. The first is given by converting the integral in equation (4) into a Riemann sum over the measured size resolved concentrations with no correction. The histogram over which the integral is summed is defined by the aerosol channel boundaries, using the new aerosol channel boundaries obtained from the CEF method. The value of the integral within each discrete size interval is calculated as the arithmetic mean of the channel boundaries. Geometric means were also tried but these results deviated further from the fitted size distributions and so were discarded. The other three calculations use equation (4) with three different derivations of the aerosol size distribution. These derivations are (1) using equation (2) with no correction to N_{ch}, as before the discovery of the calibration error (Deshler et al., 2003), (2) using equation (2) with the KD15 correction to N_{ch}, and (3) using equation (3) with $CEF_{ch}(r)$ determined by the laboratory data as described in section 3.2.

For each comparison all data from the coincidences during each period are averaged to provide a mean aerosol extinction and a population standard deviation from the satellite remote and balloon-borne in situ measurements. For each of the four comparisons at each wavelength in each period, the satellite data remain the same. The differences are in the four ways the in situ data are processed.

5.3.1. Comparisons With SAGE II Measurements of Aerosol Extinction

Figure 8 presents the results for SAGE II at 525 and 1,020 nm for the volcanic (a–d) and nonvolcanic (e–h) period. For the volcanic period the four calculations are close and follow each other reasonably well, Figures 8a–8d, except at 525 nm below 16 km. In this region there is separation between the four methods, with the explicit CEF method, black, and Riemann sum, green, in agreement but overestimating SAGE II by more than 50%. Such differences are observed at 1,020 nm between 13 and 15 km and above 26 km. Through the 16- to 28-km range at 525 nm and 15- to 26-km range at 1,020 nm the OPC estimated extinctions are all within the ±40% uncertainty expected, as shown by the gray hatched area, for all the OPC calculations. Deviations from this statement occur below 16 km and above 26 km for all but Deshler et al. (2003). None of the other fitting methods do quite as well as Deshler et al. throughout the profile, but all fitting methods are within the two-sided uncertainty of the OPC measurements except as noted above. Three of the four in situ estimates display an unusually high deviation from SAGE II in the volcanic period between 13 and 15 km at 1,020 nm. This results from a local minimum in the SAGE II averaged profile, while the in situ data remain relatively flat. This region is close to the tropopause and may result from cloud clearing or more variability with location near the tropopause. A similar deviation from SAGE II is observed at 525 nm below 16 km in the volcanic period for the CEF and Riemann sum methods.

For the nonvolcanic period, Figures 8e–8h, the standard deviations of both the remote measured, and in situ derived, extinctions are reduced considerably, as is the extinction value. The extinction axes in Figures 8e and 8g are reduced by a factor of 10 over Figures 8a and 8b. The Deshler et al. calculations consistently underestimate SAGE extinctions throughout the profile, as do Riemann sums (not shown) if the sums use the channel boundaries defined by Deshler et al. Both methods derive extinctions which are at or below the boundary of SAGE II-40%, which represents the uncertainty ascribed to the OPC derived extinctions at both wavelengths. This result, which has been noted before (Deshler et al., 2003; Hervig & Deshler, 2002), provided the motivation for the work of KD15, which discovered the calibration error discussed above. Figures 8f and 8h show clearly why this work was necessary. They also show that both the method proposed here, explicit CEF equation (3) in the figure, and the method proposed by KD15 do a reasonable
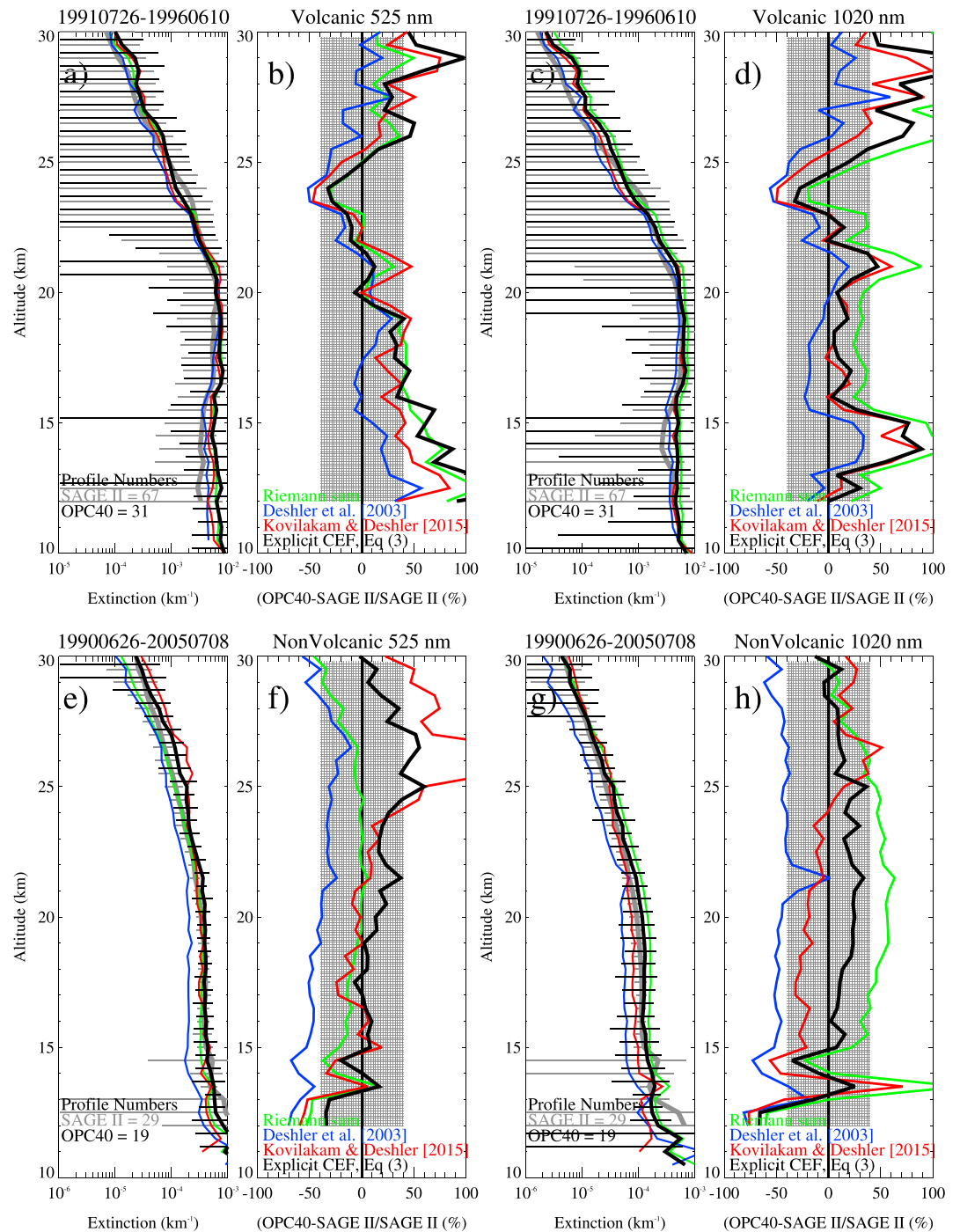
Figure 8. Altitude profiles of aerosol extinction at 525 nm, left, and 1,020 nm, right, for the volcanic period (a and c) and nonvolcanic period (e and g), as measured by SAGE II in gray and calculated from the OPC40 using four methods: Riemann sums, in green, and three lognormal size distribution retrievals: Deshler et al. (2003), blue; Kovilakam and Deshler (2015), red; and explicit CEF equation (3), this paper, black. The Deshler et al. (2003) derivations have been publicly available on the Wyoming web site. Horizontal lines in the extinction panels are population standard deviations of SAGE II in gray and OPC40 explicit CEF equation (3) in black. The extinction axes change a factor of 10 between volcanic and nonvolcanic periods. Panels (b), (d), (f), and (h) show percentage differences between calculated extinctions from the OPC40, using the four methods noted in the legends, and SAGE II. SAGE = Stratospheric Aerosol and Gas Experiment; OPC = optical particle counter; CEF = counting efficiency function.

job of making the correction, as does the Riemann sum, green lines, when the channel boundaries have been redefined from Figure 5. At 525 nm the Riemann sum, with new channel boundaries, KD15, and CEF equation (3) are in agreement with the satellite below 24 km. Above 24 km the Riemann sum, CEF equation 3, and Deshler et al. remain within 40% of SAGE II. At 1,020 nm the agreement of CEF equation 3 and KD15 with SAGE III is similar, with opposite sign, below 25 km, while CEF equation 3 is slightly better than KD15 above 25 km. The Riemann sum overestimates SAGE II in the center of the profile.

### 5.3.2. Comparisons With HALOE Measurements of Aerosol Extinction

Similar comparisons are shown in Figure 9 for the HALOE extinctions at 3.40 and 3.46 μm. For the volcanic period all the fitted methods provide extinction estimates, which are within ± 40% of the satellite measurements at altitudes above 15 km, Figures 9a–9d, and all four in situ estimates show a trend from overestimating HALOE below 20 km to underestimating HALOE above 25 km. KD15 and equation (3) are mostly in agreement with each other and systematically larger than Deshler et al. Compared to HALOE, KD15 and equation (3) are worse than Deshler et al. below 22 km, but better above. The Riemann sum significantly overestimates HALOE measured extinction below 23 km. Similar to SAGE the in situ estimates all over estimate HALOE below 15 km, which is driven primarily by a significant decrease in the HALOE extinctions. This is probably related to cloud clearing and other problems near the tropopause (Thomason, 2012).

The nonvolcanic results, Figures 9e–9h, show the same pattern as with SAGE II. Deshler et al. is just at or below the HALOE-40% measurement, and in this case the Riemann sums follow Deshler et al. This underestimation highlights again the problem motivating this work and KD15. As with the volcanic cases KD15 and explicit CEF equation (3) estimates track each other closely. Both reproduce well the HALOE extinctions, particularly between 15 and 24 km. Above 24 km both these size distributions under estimate HALOE, while they overestimate HALOE below 15 km. All fitted distributions show a large deviation from HALOE below 15 km at 3.46 μm, caused primarily by a decrease in HALOE.

The comparisons shown in Figures 8 and 9 all use altitude as the reference, but only for measurements above the OPC40 determined tropopause, which ranged from less than 10 to over 16 km. The variations in tropopause height effectively reduces the stated number of comparisons on the figures. Below 12.5 km, for example, the number of comparisons is reduced by 40–50% because of in situ profiles with a higher tropopause. Because of this reduction and the significant discrepancies between in situ and remote measurements below 15 km, the data were recompared using a tropopause relative height. For this the lapse rate tropopause determined from the in situ data was assumed to also apply to the corresponding satellite data, and the data were then compared with this tropopause relative height, effectively moving comparisons that may have formerly appeared at >13 km to a point just above the tropopause relative height and increasing the number of comparisons in this region. The comparisons are shown in Figure 10 for the volcanic period for SAGE II (a–d) and HALOE (e–h). While the low-altitude discrepancies are not eliminated they are significantly reduced.

For SAGE II, Figures 10a–10d, the overestimation of OPC40, up to 5 km above the tropopause, is reduced from over 100% to near 75% at 525 nm and to generally within the precision of the OPC at 1,020 nm. For the nonvolcanic period, not shown, when the agreement was already reasonable the picture does not change. Similar improvements are seen for HALOE in the volcanic period, Figures 10e–10h. The comparisons decrease from well over 100% overestimation by the OPC40 at altitudes less than 15 km to less than 100% difference from 2 to 5 km above the tropopause. In the nonvolcanic period, not shown, the differences decrease from near to over 100% to generally within the precision of the OPC for the tropopause relative comparisons. These reductions in the comparison discrepancies exhibited by the tropopause relative analysis may be further limited by using a potential temperature/potential vorticity coordinate system, but such an analysis is beyond the scope of this work.

Clearly, the corrections to the calibration error have the most impact during the nonvolcanic period while causing smaller changes during the volcanic period (Figures 8 and 9). Retaining minimal changes to the in situ profiles during the volcanic period is important since the old size distribution fitting method (Deshler et al., 2003) already provided reasonable agreement with the satellite data. Achieving a similar result using the correction method proposed by KD15 required some tuning of an empirical parameter, using SAGE II as a reference. For the work presented here, agreement of the in situ estimates and satellite measurements is achieved without requiring any factors external to the in situ measurements and their laboratory analysis.
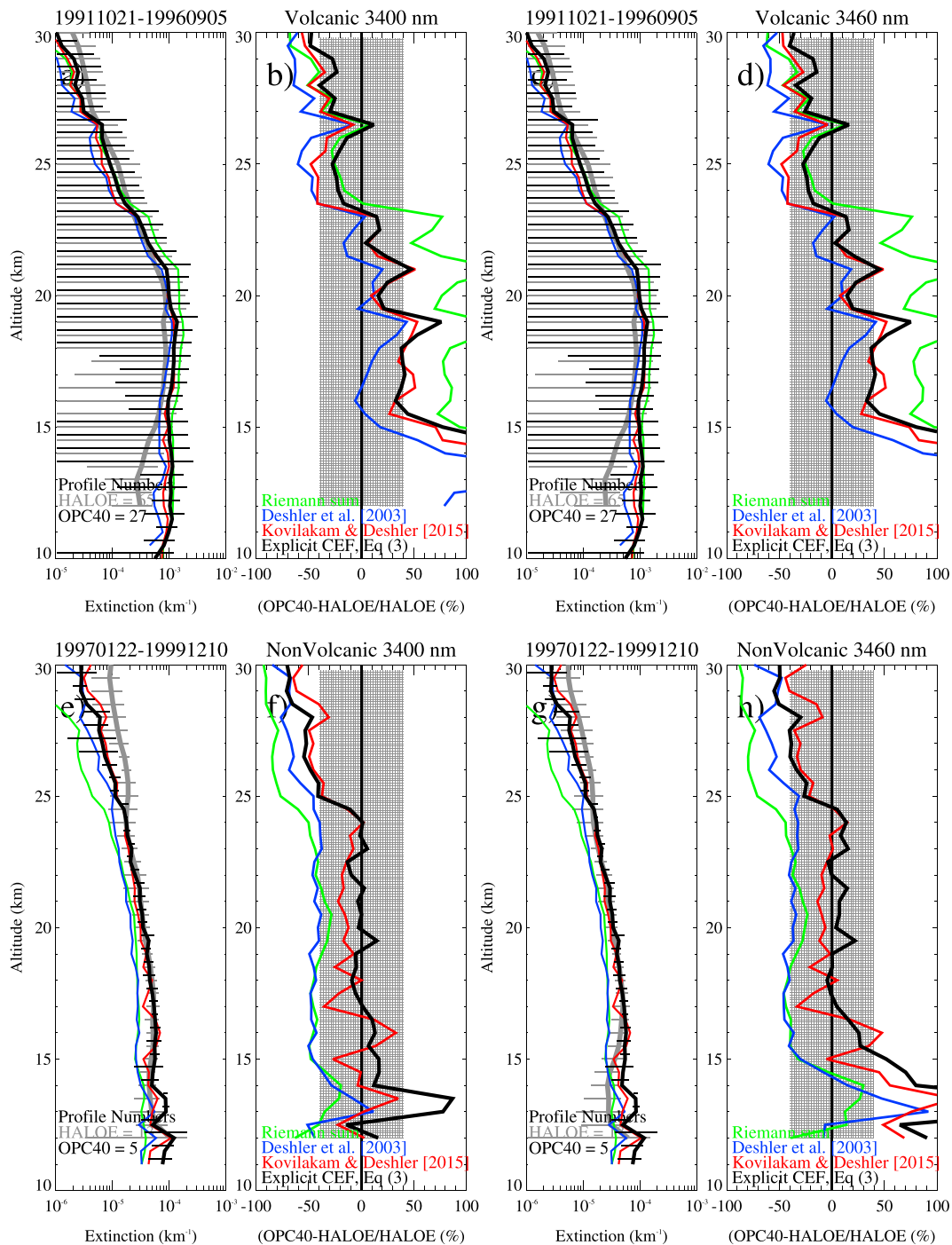
Figure 9. Same as Figure 8 except for measurements at 3,400 and 3,460 nm by HALOE. The number of HALOE measurements in the nonvolcanic period is 13. HALOE = Halogen Occultation Experiment.

The real difference appears in the comparisons in the nonvolcanic period. Here there are clear improvements in the agreement of the in situ estimates of extinction with both SAGE II and with HALOE, while the Deshler et al. estimates remain on the satellite-40% boundary. There are not a lot of differences between KD15 and explicit CEF for HALOE or SAGE II. Both are in reasonable agreement with the satellites from 15 to 25 km.
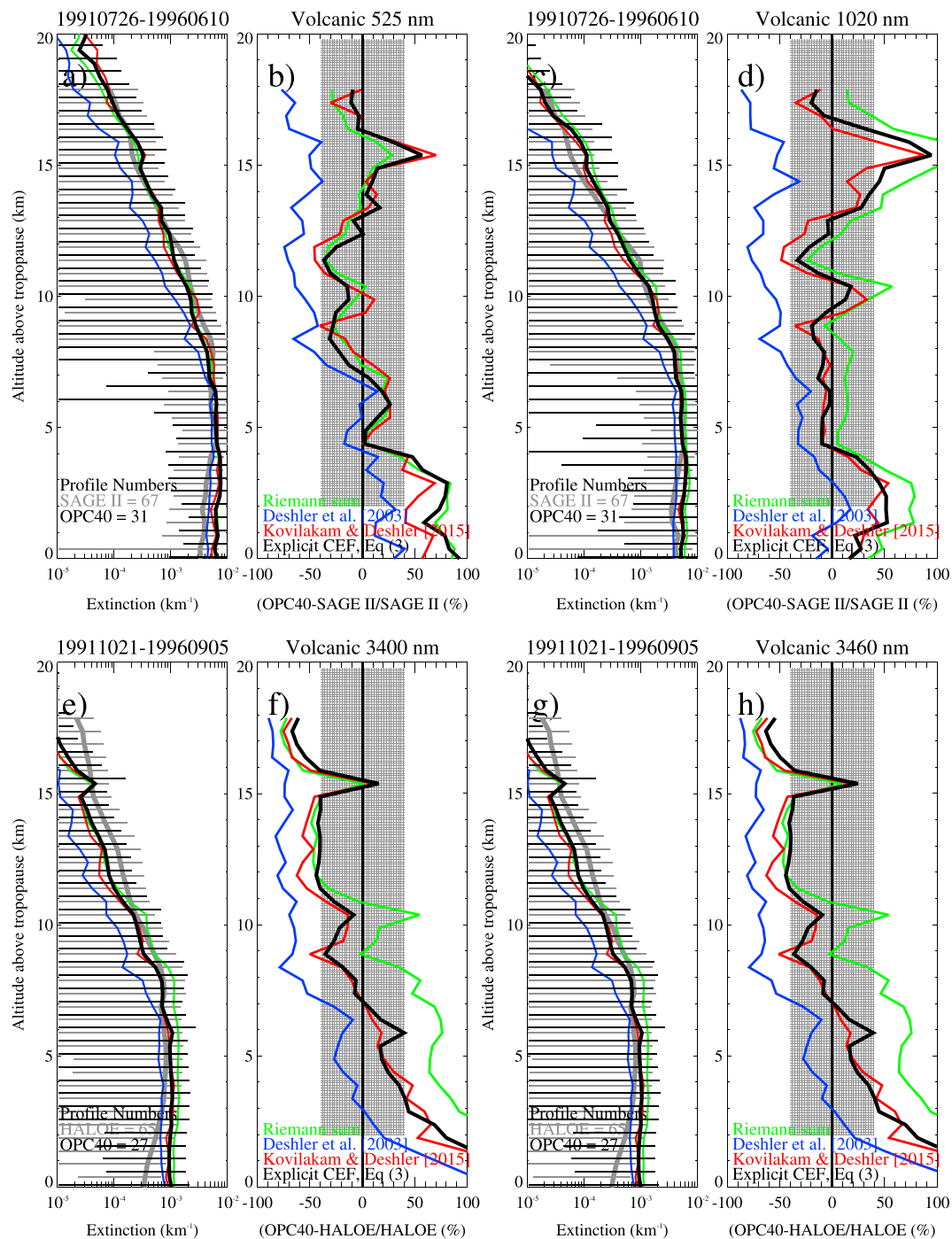
Figure 10. Same as Figures 8 and 9 for the volcanic comparisons for SAGE II (a–c) and HALOE (d–h) except with the reference altitude switched to tropopause relative altitude.

The agreement of extinctions estimates from the OPC40 data using the explicit CEF, equation (3), with the SAGE II and HALOE measured extinctions provides strong support for the new size distribution retrieval method described here. The improvement in this agreement over the method of Deshler et al. (2003) is particularly significant in the nonvolcanic case for the comparisons with both satellites. Similar improvements in comparisons with SAGE II at 386 and 452 nm in the nonvolcanic period are also found, not shown. The agreement of in situ extinction estimates with measured satellite extinctions, between 386 and 3,460 nm, indicates that the new CEF fitting method does an adequate job handling the in situ data gap between

0.01 and 0.15 μm. While not definitive, this result provides confidence in the accuracy of the in situ estimates of SAD and volume density, providing a strong point of comparison for satellite estimates of these quantities.

5.4. Aerosol SAD Estimates: Comparing SAGE II and HALOE With OPC40

The comparisons of the satellite and in situ estimates of aerosol SAD are shown in Figure 11 for SAGE II and HALOE in the volcanic period (a–d) and nonvolcanic period (e–h). The SAGE II v7.0 estimates of SAD are described in Thomason et al. (2008) and the HALOE SADs are those developed by Hervig and Deshler (1998). The difference plots in Figure 11 use the in situ data as the reference, so the axis is (satellite-in situ)/in situ. In this case the Riemann sum estimates of aerosol SAD are highly deficient, underestimating the satellite estimates by well over 100%, which is outside the plot boundaries. The cause of this divergence is the importance of small particles when estimating SAD. A Riemann sum is incapable of resolving the region between 0.01 and 0.15 μm, providing striking evidence of the need for fitted size distributions to interpret in situ aerosol measurements, which have little size resolution below 0.1 μm. The importance of the small particles in SAD is also the reason most satellite estimates of SAD are challenged in nonvolcanic periods since they are also not sensitive to particles <0.1 μm. The sensitivity of extinction to the larger particles is why the Riemann sums do fairly well in the extinction comparisons.

The comparisons with SAGE II and HALOE during the volcanic period (Figures 11a–11d) are quite similar, indicating the satellites systematically overestimate the Deshler et al. (2003) estimates above 23 km, while they reproduce well the KD15 and explicit CEF results throughout much of the profile, and almost always the satellite is within ±40% of the in situ estimates. In this period there is almost no differentiation between KD15 and explicit CEF results.

In the nonvolcanic period there are distinct differences in how the satellites compare with the in situ estimates. SAGE II overestimates the Deshler et al. results but is in reasonable agreement with KD15 and explicit CEF between 17 and 28 km. Below 17 km SAGE II hovers around 40% below the CEF estimates. For HALOE the picture is different. HALOE is consistent with Deshler et al. throughout the profile, while it underestimates SAD in comparison to KD15 and CEF, which are both in agreement, while HALOE is right at the boundary of in situ-40% for these two in situ estimates. That HALOE is in closest agreement with the Deshler et al. (2003) estimates of aerosol SAD is perhaps not surprising since this method figured prominently in the methods used to estimate HALOE aerosol SAD (Hervig & Deshler, 1998).

6. Discussion

To account for the calibration error described by KD15 and in section 2.2, and thus to correct the 20 plus years of in situ OPC40 aerosol measurements, there are two basic approaches: (1) modify the measured aerosol concentrations to reflect the new counting efficiency or (2) modify the reported aerosol sizes to those that are appropriate for a 50% collection efficiency based on laboratory data. The first approach was that adopted by KD15. This approach has some difficulties as discussed in KD15. The number concentrations cannot all be corrected by a simple factor of 2, to correct the 25% counting efficiency to a 50% counting efficiency. Rather, the correction factor must depend on the shape of the size distribution. For example, in the case of a flat cumulative aerosol size distribution, the number concentration at two sizes ($r_a < r_b$) will be the same, $N(r > r_a) = N(r > r_b)$. Correcting $N(r > r_a)$ by a factor of 2 is incorrect since the channel at r_a has already counted all the particles larger than r_a, since, in this case, all particles are also larger than r_b. That led KD15 to propose a scheme with a correction factor for aerosol number concentration weighted by the rough aerosol size distribution, reflected in the measurements. In broad regions of a size distribution, where dN/dr is small, the correction factor is nearer to 1. For narrow distributions in the regions which are steep, where dN/dr is large, the correction factor is near or at the limit of 2. This fact is the reason the problem identified in KD15 was not so apparent in the volcanic post Pinatubo period, when size distributions were fairly broad, but did appear in the nonvolcanic period when size distributions became narrower and steeper at the OPC measured sizes. Thus, any correction scheme must cause minimal differences in broad regions of a size distribution and primary difference in narrow steep regions. In approach (2) this is handled by the adjustments in the reported sizes. For broad distributions changing the reported size to somewhat larger particles may not have much impact, while in narrow and steep regions changing the reported sizes will have a significant impact in moving the moments of the fitted size distributions to larger sizes (Figure 7).
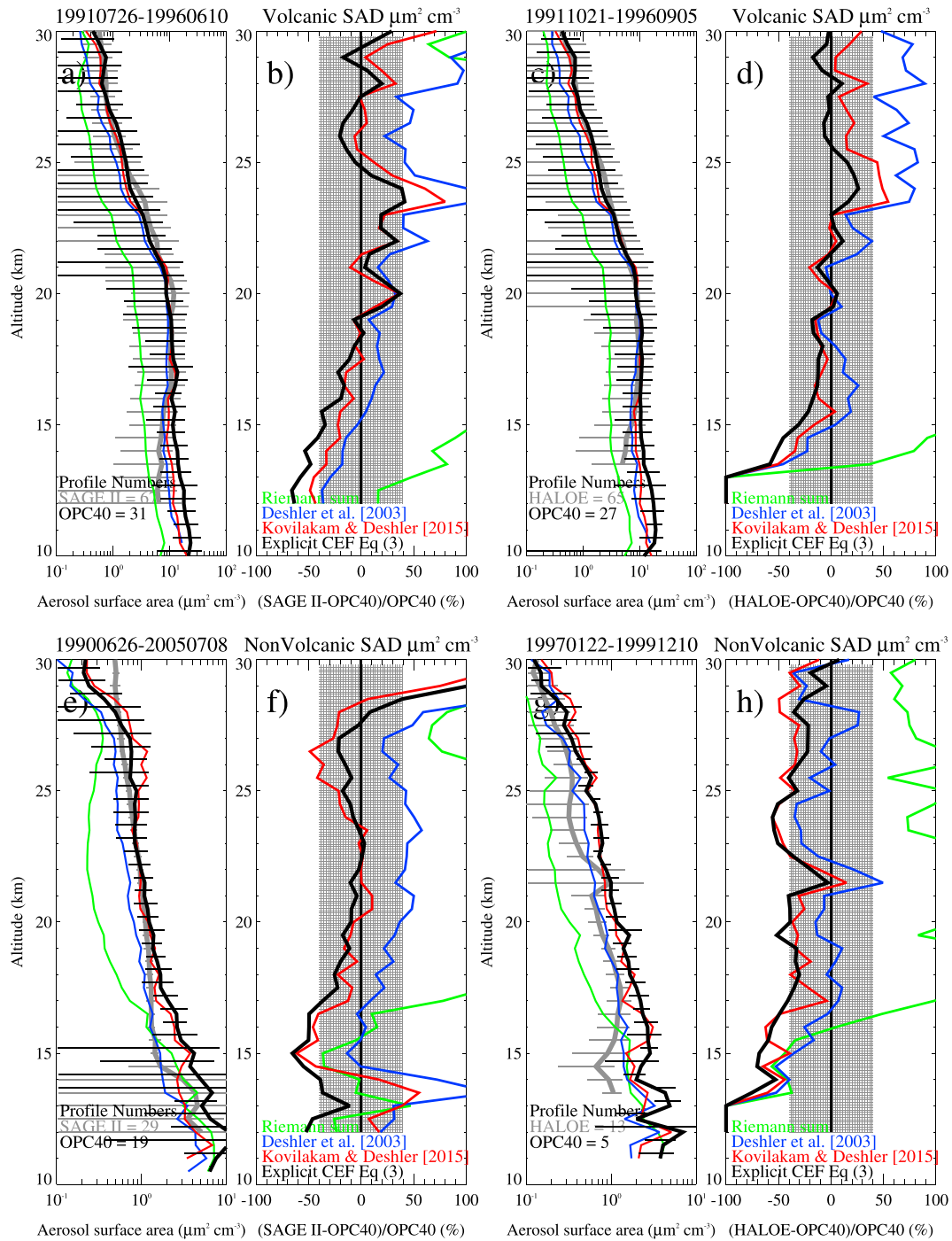
Figure 11. Profiles of surface area density (SAD) estimates from Stratospheric Aerosol and Gas Experiment (SAGE) II, left, and Halogen Occultation Experiment (HALOE), right, compared to in situ estimates using four methods to handle the in situ data described in Figure 8 and listed in the legend in panels (b), (d), (f), and (h). Panels (a)–(d) for the volcanic period and (e–h) for the nonvolcanic period. The SAD axes bottom row are reduced by a factor of 10 from the top row. Horizontal lines in the extinction panels are population standard deviations of SAGE II in gray and OPC40 explicit counting efficiency function (CEF) in black. Differences of the satellite estimates compared to the in situ estimates for the Riemann sum and three possible size distribution retrievals are shown in panels (b), (d), (f), and (h), following the style of Figures 8 and 9 except now using the OPC40 as the reference.

The approach adopted here is option (2): to modify the reported aerosol sizes to reflect the true 50% counting efficiency for each aerosol channel. The advantage of this method is that the fundamental measurement of the instrument, the pulse count rate, which is converted to aerosol number concentration, is not modified, but rather, the size ascribed to that particular aerosol number concentration is changed. For an OPC the aerosol channel sizes are prescribed during instrument design. The calibration procedure is then developed for the prescribed aerosol channels. Once an instrument is calibrated, it can be checked for a proper calibration with counting efficiency tests such as described in section 3. At the time of the development of the OPC40, in the late 1980s, facilities to complete such counting efficiency tests were not available. The facilities used by KD15, to check the calibration of the OPC40 and OPC25 instruments, became available in the 2000s. With these facilities KD15 were able to confirm that the calibration error they described, and discussed in section 2 of this paper, was the primary issue driving the discrepancy between the satellite measured and in situ estimated aerosol extinction during the nonvolcanic period. Following approach (2), the primary change to the data will be the aerosol sizes assigned to the various channels of the OPC40.

With such a change in the reported aerosol sizes, and if the counting efficiency curves were steep, such as in Figure 6 for the OPC25, the analysis software to derive lognormal aerosol size distributions from the measurements (Deshler et al., 2003) could be applied with little modification. However, the counting efficiency curves of the OPC40 are significantly shallower than the OPC25, suggesting that the number of counts registered at any one channel arises from a fairly wide range of particle sizes surrounding the channel, Figure 5. In this case the implicit CEF (0 for $r < \mu_{50}$(ch), 1 for $r \geq \mu_{50}$(ch)) in the derivation of aerosol size distribution, equation (2), is not appropriate. Rather, a better solution is achieved by using the laboratory data, Figure 5, and including an explicit CEF in the derivation of aerosol size distribution, equation (3). In this case, in addition to reporting the modified aerosol size for each OPC channel, which constitutes the median of the CEF describing the laboratory data, μ_{50}, the width of the CEF, σ_{OPC}, must also be included, and for completeness the functional form of the CEF, equation (1). While this increases the complexity of the retrieval of aerosol size distributions from the measurements, the advantages are the following: (1) The fundamental measurement of the OPC40, the number concentration, is not modified. (2) Laboratory data describing the counting efficiency of the instrument are fully applied. (3) There is no dependence of the method on an intrinsic aerosol size distribution, thus no need to differentiate between volcanic and nonvolcanic periods. (4) The approach is intrinsically satisfying since it relies on a complete description of the mathematics behind aerosol size distribution retrievals.

Figures 8 and 9 display comparisons between satellite measurements of aerosol extinction and in situ estimates based on a Riemann sum of the measurements and three derived aerosol size distributions: Deshler et al. (2003), KD15, and explicit CEF, equation (3). These figures clearly show the discrepancies, discussed above, between satellite measurements and in situ estimates of aerosol extinction from Deshler et al. (2003), in the nonvolcanic period. The figures also show that both correction methods, KD15 and explicit CEF, do not significantly change the previous results in the volcanic period, with the exception of the 525-nm comparison below 16 km, although this result partly arises from using altitude rather than tropopause relative altitude as the reference, Figure 10. In contrast in the nonvolcanic period there is a significant improvement, such that the in situ estimates of aerosol extinction are now, within their uncertainty bounds, primarily in agreement with the satellite measurements. While throughout most profiles the two correction methods are in fairly close agreement, where there is disagreement, the explicit CEF results are a bit better: less abrupt changes in the profiles, slightly better agreement with the satellite measurements.

Figure 11 follows the style of Figures 8 and 9 in comparisons of SAGE II and HALOE estimates of aerosol SAD with the Riemann sum and the three methods for deriving aerosol size distributions. Similar to the extinction comparisons, the two new methods track each other closely and in general the satellite estimates of aerosol SAD are in better agreement with estimates of SAD from these two size distributions than with the SAD from the Deshler et al. size distributions, particularly for SAGE II and HALOE in the volcanic period. The HALOE comparisons of SAD in the nonvolcanic period are the exception to these general conclusions. In this case, HALOE is at the lower boundary of the two new in situ estimates of SAD, while in agreement with the SAD estimates from the Deshler et al. size distributions.

The conclusions of this analysis are clear. The explicit CEF method provides the best option for deriving aerosol size distributions from the Wyoming balloon-borne in situ measurements using the OPC40

instrument. The CEF method is based on a fundamental mathematical statement of the problem. It does not have to explicitly account for the calibration error associated with the OPC40. It can be applied to any OPC for which counting efficiency curves are available, thus to the OPC25 and the laser based OPC described by Ward et al. (2014). It provides results that are substantially equivalent to the corrections suggested by KD15, thus displaying the capability to account for the calibration error of the OPC40. Where these two methods diverge, the CEF method is usually in better agreement with the satellite measurements for aerosol extinction or the satellite measurements are in better agreement with the CEF results for SAD. Finally, the explicit CEF method leaves the fundamental OPC measurements of number concentration untouched while fully taking advantage of all the information available from the laboratory measurements of counting efficiency.

7. Summary and Conclusions

An unexplained discrepancy, during nonvolcanic periods, between SAGE II measurements of aerosol extinction and estimates from balloon-borne in situ measurements prompted a thorough analysis of the in situ measurements which led to the discovery of a fundamental error in the calibration of the Wyoming OPCs, OPC40s, in use from 1991 to 2012 (KD15). The calibration error meant that the counting efficiency at the reported aerosol sizes of the OPC40 was not the expected 50%, but closer to 25%. To correct for this error, KD15 proposed a scheme to correct the number concentrations reported for the OPC40 measurements. Concerns about the appropriateness of this method led to the work here and to revisiting the laboratory data of KD15. In this reanalysis these data are used to derive CEFs, as the integrals of the Gaussian distributions, which reflect the differential counting efficiency surrounding an aerosol channel. The derived CEFs represent the cumulative counting efficiency measured in the laboratory at each OPC channel. These CEFs were then used as an explicit component in a new method to derive the unimodal/bimodal lognormal size distributions which characterize the OPC40 measurements.

To assess the value of this new, explicit CEF, method to analyze the OPC40 measurements, moments of the aerosol size distribution, aerosol extinction and aerosol SAD, were compared to the previous results of (Deshler et al., 2003) and to the results of KD15, who used the Deshler et al. method to derive aerosol size distributions after correcting the OPC40 number concentration measurements. The aerosol moments obtained from these three size distribution retrieval methods, plus a simple Riemann sum, were compared to measurements of aerosol extinction from SAGE II (525 and 1,020 nm) and HALOE (3.40 and 3.46 μm) and with SAGE II and HALOE estimates of aerosol SAD. The new explicit CEF method was found to (1) agree with or improve upon the results from Kovilakam and Deshler (2015) in improving the agreement of derived aerosol extinction with SAGE II and HALOE measurements in the nonvolcanic period, (2) limit the deviation from the old method in the volcanic period, when that method was in good agreement with the satellite measurements, (3) not require any modification of the number concentration measurements from the OPC40, (4) account for the calibration error of the OPC40 without requiring any a priori dependence on the intrinsic aerosol size distribution, and (5) be applicable to any OPC for which counting efficiency curves are available. The agreement of this new analysis with the SAGE II and HALOE measurements strengthens both data sets and allows the possibility for the in situ measurements to inform satellite retrievals of geophysical moments of the aerosol size distribution, for example, surface area and volume densities.

The conclusions of this work are to

1. Modify the sizes of the aerosol channels reported for the OPC40 and OPC25 measurements.
2. Include in the data file the widths of the CEFs used to describe the counting efficiency at each channel.
3. Retrieve aerosol size distributions from the measurements using an explicit CEF in the integral used to describe the measurements, the expression from which the relevant aerosol size distributions are derived.
4. Apply this method with an explicit CEF to all size distributions derived from the Wyoming measurements.
5. Require that counting efficiency measurements be completed for all future instruments designed to extend the Wyoming record of in situ stratospheric aerosol measurements.

The new data files and size distributions from this work are available at the web site hosting the Wyoming in situ data (http://www.atmos.uwyo.edu/~Deshler/Data/Aer_Meas_Wy_read_me.htm). The new data are located in a folder identified as UWv2.0 with the original data designated in a folder as UWv1.0.

References

Adriani, A., Deshler, T., Di Donfrancesco, G., & Gobbi, G. P. (1995). Polar stratospheric clouds and volcanic aerosol during 1992 spring over McMurdo Station, Antarctica: Lidar and particle counter comparisons. *Journal of Geophysical Research*, *100*, 25,877–25,898.

Arnold, F., Curtius, J., Spreng, S., & Deshler, T. (1998). Stratospheric aerosol sulfuric acid: First direct in situ measurements using a novel balloon-based mass spectrometer apparatus. *Journal of Atmospheric Chemistry*, *30*, 3–10.

Baron, P. A., & Willeke, K. (2005). *Aerosol measurement: Principles, techniques, and applications*, (2nd ed.). Wiley-Interscience.

Borrmann, S., Kunkel, D., Weigel, R., Minikin, A., Deshler, T., Wilson, J. C., et al. (2010). Aerosols in the tropical and subtropical UT/LS: in-situ measurements of submicron particle abundance and volatility. *Atmospheric Chemistry and Physics*, *10*, 5573–5592. https://doi.org/10.5194/acp-10-5573-2010

Borrmann, S., Thomas, A., Rudakov, V., Yushkov, V., Lepuchov, B., Deshler, T., et al. (2000). Stratospheric aerosol measurements in the Arctic winter of 1996/1997 with the M-55 Geophysika high-altitude research aircraft. *Tellus*, *52B*, 1088–1103.

Bourassa, A. E., Degenstein, D. A., Gattinger, R. L., & Llewellyn, J. E. (2007). Stratospheric aerosol retrieval with optical spectrograph and infrared imaging system limb scatter measurements. *Journal of Geophysical Research*, *112*, D10217. https://doi.org/10.1029/2006JD008079

Campbell, P., & Deshler, T. (2014). Condensation nuclei measurements in the midlatitude (1982–2012) and Antarctic (1986–2010) stratosphere between 20 and 35 km. *Journal of Geophysical Research: Atmospheres*, *119*, 137–152. https://doi.org/10.1002/2013JD019710

Chu, W. P., McCormick, M. P., Lenoble, J., Brogniez, C., & Pruvost, P. (1989). SAGE II inversion algorithm. *Journal of Geophysical Research*, *94*(D6), 8339–8351. https://doi.org/10.1029/JD094iD06p08339

Damadeo, R. P., Zawodny, J. M., Thomason, L. W., & Iyer, N. (2013). SAGE version 7.0 algorithm: Application to SAGE II. *Atmospheric Measurement Techniques*, *6*, 3539–3561. https://doi.org/10.5194/amt-6-3539-2013

Deshler, T., Hervig, M. E., Hofmann, D. J., Rosen, J. M., & Liley, J. B. (2003). Thirty years of in situ stratospheric aerosol size distribution measurements from Laramie, Wyoming (41°N), using balloon-borne instruments. *Journal of Geophysical Research*, *108*(D5), 4167. https://doi.org/10.1029/2002JD002514

Deshler, T., Johnson, B. J., & Rozier, W. R. (1993). Balloonborne measurements of Pinatubo aerosol during 1991 and 1992 at 41°N, vertical profiles, size distribution, and volatility. *Geophysical Research Letters*, *20*, 1435–1438.

Deshler, T., Johnson, B. J., & Rozier, W. R. (1994). Changes in the character of polar stratospheric clouds over Antarctica in 1992 due to the Pinatubo volcanic aerosol. *Geophysical Research Letters*, *21*, 273–276.

Deshler, T., & Oltmans, S. J. (1998). Vertical profiles of volcanic aerosol and polar stratospheric clouds above Kiruna, Sweden: Winters 1993 and 1995. *Journal of Atmospheric Chemistry*, *30*, 11–23.

Deshler, T. B., Nardi, A., Adriani, F., Cairo, G., Hansen, F., Fierli, A. H., & Pulvirenti, L. (2000). Determining the index of refraction of polar stratospheric clouds above Andoya (69°N) by combining size-resolved concentration and optical scattering measurements. *Journal of Geophysical Research*, *105*, 3943–3953.

Eidhammer, T. (2006), Determining particle index of refraction with measurements of scattering at two angles. Ph.D. thesis, 136 pages, University of Wyoming, Laramie.

Friberg, J., Martinsson, B. G., Andersson, S. M., Brenninkmeijer, C. A. M., Hermann, M., Van Velthoven, P. F. J., & Zahn, A. (2014). Sources of increase in lowermost stratospheric sulphurous and carbonaceous aerosol background concentrations during 1999–2008 derived from CARIBIC flights. *Tellus*, *66*(1). https://doi.org/10.3402/tellusb.v66.23428

Granqvist, C. G., & Buhrman, R. A. (1976). Log-normal size distributions of ultrafine metal particles. *Solid State Communications*, *18*, 123–126.

Günther, A., Höpfner, M., Sinnhuber, B.-M., Griessbach, S., Deshler, T., von Clarmann, T., & Stiller, G. (2018). MIPAS observations of volcanic sulfate aerosol and sulfur dioxide in the stratosphere. *Atmospheric Chemistry and Physics*, *18*(2), 1217–1239. https://doi.org/10.5194/acp-18-1217-2018

Hanson, D. R., Ravishankara, A. R., & Solomon, S. (1994). Heterogeneous reactions in sulfuric acid aerosols: A framework for model calculations. *Journal of Geophysical Research*, *99*(D2), 3615–3629. https://doi.org/10.1029/93JD02932

Hervig, M. E., & Deshler, T. (1998). Stratospheric aerosol surface area and volume inferred from HALOE, CLAES, and ILAS measurements. *Journal of Geophysical Research*, *103*, 25,345–25,352.

Hervig, M. E., & Deshler, T. (2002). Evaluation of aerosol measurements from SAGE II, HALOE, and balloonborne optical particle counters. *Journal of Geophysical Research*, *107*(D3), 4031. https://doi.org/10.1029/2001JD000703

Hervig, M. E., Russell, J. M. III, Gordley, L. L., Park, J. H., Drayson, S. R., & Deshler, T. (1996). Validation of aerosol measurements made by the Halogen Occultation Experiment. *Journal of Geophysical Research*, *101*, 10,267–10,276.

Hirschman, I. I., & Widder, D. V. (1955). *The Convolution Transform*. Princeton, NJ: Princeton University Press.

Hofmann, D. J. (1990). Increase in the stratospheric background sulfuric acid aerosol mass in the past 10 years. *Science*, *248*, 996–1000.

Hofmann, D. J. (1993). Twenty years of balloon-borne tropospheric aerosol measurements at Laramie, Wyoming. *Journal of Geophysical Research*, *98*, 12,753–12,766.

Hofmann, D. J., & Deshler, T. (1991). Stratospheric cloud observations during formation of the Antarctic ozone hole in 1989. *Journal of Geophysical Research*, *96*, 2897–2912.

Hofmann, D. J., & Rosen, J. M. (1982). Balloon-borne observations of stratospheric aerosol and condensation nuclei during the year following the Mt. St. Helens eruption. *Journal of Geophysical Research*, *87*, 11,039–11,061.

Hofmann, D. J., Rosen, J. M., Pepin, T. J., & Pinnick, R. G. (1975). Stratospheric aerosol measurements, I, Time variations at northern midlatitudes. *Journal of the Atmospheric Sciences*, *32*, 1446–1456.

Hurst, D. F., Oltmans, S. J., Vömel, H., Rosenlof, K. H., Davis, S. M., Ray, E. A., et al. (2011). Stratospheric water vapor trends over Boulder, Colorado: Analysis of the 30 year Boulder record. *Journal of Geophysical Research*, *116*, D02306. https://doi.org/10.1029/2010JD015065

Jäger, H. (2005). Long-term record of lidar observations of the stratospheric aerosol layer at Garmisch-Partenkirchen. *Journal of Geophysical Research*, *110*, D08106. https://doi.org/10.1029/2004JD005506

Jäger, H., & Hofmann, D. (1991). Midlatitude lidar backscatter to mass, area, and extinction conversion model based on in situ aerosol measurements from 1980 to 1987. *Applied Optics*, *30*, 127–138.

Jonsson, H. H., Wilson, J. C., Brock, C. A., Knollenberg, R. G., Newton, R., Dye, J. E., et al. (1995). Performance of a focused cavity aerosol spectrometer for measurements in the stratosphere of particle size in the 0.06–2.0 μm diameter range. *Journal of Atmospheric and Oceanic Technology*, *12*, 115–129.

Junge, C. E., Changnon, C. W., & Manson, J. E. (1961). Stratospheric aerosols. *Journal of Meteorology*, *18*, 81–108.

Khaykin, S. M., Godin-Beekmann, S., Keckhut, P., Hauchecorne, A., Jumelet, J., Vernier, J.-P., et al. (2017). Variability and evolution of the midlatitude stratospheric aerosol budget from 22 years of ground-based lidar and satellite observations. *Atmospheric Chemistry and Physics*, *17*, 1829–1845. https://doi.org/10.5194/acp-17-1829-2017

Kovilakam, M., & Deshler, T. (2015). On the accuracy of stratospheric aerosol extinction derived from in situ size distribution measurements and surface area density derived from remote SAGE II and HALOE extinction measurements. *Journal of Geophysical Research: Atmospheres*, *120*, 8426–8447. https://doi.org/10.1002/2015JD023303

Kremser, S., Thomason, L. W., von Hobe, M., Hermann, M., Deshler, T., Timmreck, C., et al. (2016). Stratospheric aerosol - Observations, processes, and impact on climate. *Reviews of Geophysics*, *54*, 278–335. https://doi.org/10.1002/2015RG000511

Lambert, A., Grainger, R. G., Remedios, J. J., Reburn, W. J., Rodgers, C. D., Taylor, F. W., et al. (1996). Validation of aerosol measurements from the improved stratospheric and mesospheric sounder. *Journal of Geophysical Research*, *101*, 9811–9830.

Luo, B., Krieger, U., & Peter, T. (1996). Densities and refractive indices of H2SO4/HNO3/H2O solutions to stratospheric temperatures. *Geophysical Research Letters*, *23*, 3707–3710. https://doi.org/10.1029/96GL03581

Mauldin, L. E. III, Zaun, N. H., McCormick, M. P., Guy, J. H., & Vaughan, W. R. (1985). Stratospheric Aerosol and Gas Experiment II instrument: A functional description. *Optical Engineering*, *24*, 307–312.

McCormick, M. P., Hamill, P., Pepin, T. J., Chu, W. P., Swissler, T. J., & McMaster, L. R. (1979). Satellite studies of the stratospheric aerosol. *Bulletin of the American Meteorological Society*, *60*, 1038–1046.

Miao, Q. (2001), An analysis of errors associated with the measurement of aerosol concentration in situ with optical particle counters, M. S. thesis, 71 pp., University of Wyoming, Laramie.

Mishchenko, M. I., Travis, L. D., & Mackowski, D. W. (1996). T–matrix computations of light scattering by nonspherical particles: A review. *Journal of Quantitative Spectroscopy and Radiative Transfer*, *55*, 535–575.

Morse, P. M., & Feshbach, H. (1953). *Methods of Theoretical Physics, Part I*, (pp. 464–465). New York: McGraw-Hill.

Murphy, D. M., Thomson, D. S., & Mahoney, M. J. (1998). In situ measurements of organics, meteoritic material, mercury, and other elements in aerosols at 5 to 19 kilometers. *Science*, *282*, 1664–1669.

Oesburg, F. (1972). The influence of the aperture on the optical system of aerosol particle counters on the response curve. *Journal of Aerosol Science*, *3*, 307–311.

Palmer, K. F., & Williams, D. (1975). Optical constants of sulfuric acid: Application to the clouds of Venus? *Applied Optics*, *14*, 208–219.

Pinnick, R. G., Carroll, D. E., & Hofmann, D. J. (1976). Polarized light scattered from monodisperse randomly oriented nonspherical aerosol particles: Measurements. *Applied Optics*, *15*, 384–393.

Pinnick, R. G., & Hofmann, D. J. (1973). Efficiency of light-scattering aerosol particle counters. *Applied Optics*, *12*, 2593–2597.

Pinnick, R. G., Rosen, J. M., & Hofmann, D. J. (1973). Measured light scattering properties of individual aerosol particles compared to Mie scattering theory. *Applied Optics*, *12*, 37–41.

Pueschel, R. F., Russell, B., Allen, D. A., Ferry, G. V., & Snetsinger, K. G. (1994). Physical and optical properties of the Pinatubo volcanic aerosol: Aircraft observations with impactors and a Sun-tracking photometer. *Journal of Geophysical Research*, *99*, 12,915–12,922. https://doi.org/10.1029/94JD00621

Pueschel, R. F., Snetsinger, K. G., Russell, P. B., Kinne, S. A., & Livingston, J. M. (1992). The effects of the 1991 Pinatubo volcanic eruption on the optical and physical properties of stratospheric aerosols. In S. Keevalik (Ed.), *Proceedings of IRS92: Current Problems in Atmospheric Radiation*, (pp. 183–186). Hampton, Va: A. Deepak.

Reeves, J. M., Wilson, J. C., Brock, C. A., & Bui, T. P. (2008). Comparison of aerosol extinction coefficients, surface area density, and volume density from SAGE II and in situ aircraft measurements. *Journal of Geophysical Research*, *113*, DI1202. https://doi.org/10.1029/2007JD009357

Rosen, J. M. (1964). The vertical distribution of dust to 30 km. *Journal of Geophysical Research*, *69*, 4673–4676.

Rosen, J. M. (1971). The boiling point of stratospheric aerosols. *Journal of Applied Meteorology*, *16*, 52–56.

Rosen, J. M., & Hofmann, D. J. (1986). Optical modeling of stratospheric aerosols: Present status. *Applied Optics*, *25*, 410–419.

Rosen, J. M., Hofmann, D. J., & Kaselau, K. H. (1978). Vertical profiles of condensation nuclei. *Journal of Applied Meteorology*, *17*, 1737–1740. https://doi.org/10.1175/1520-0450(1978)017

Rosen, J. M., Hofmann, D. J., & Laby, J. (1975). Stratospheric aerosol measurements II: The worldwide distribution. *Journal of the Atmospheric Sciences*, *32*, 1457–1462.

Russell, J. M. III, Gordley, L. L., Park, J. H., Drayson, S. R., Hesketh, W. D., Cicerone, R. J., et al. (1993). The halogen occultation experiment. *Journal of Geophysical Research*, *98*, 10,777–10,797. https://doi.org/10.1029/93JD00799

Steele, H. M., & Hamill, P. (1981). Effects of temperature and humidity on the growth and optical properties of sulphuric acid-water droplets in the stratosphere. *Journal of Aerosol Science*, *12*, 517–528.

Sugita, T., Kondo, Y., Koike, M., Kanada, M., Toriyama, N., Nakajima, H., et al. (1999). Balloon-borne optical counter for in situ aerosol measurement. *Journal of Atmospheric Chemistry*, *32*, 183–204.

Thomason, L. W. (2012). Toward a combined SAGE II-HALOE aerosol climatology: An evaluation of HALOE version 19 stratospheric aerosol extinction coefficient observations. *Atmospheric Chemistry and Physics*, *12*(17), 8177–8188.

Thomason, L. W., Burton, S. P., Luo, B.-P., & Peter, T. (2008). SAGE II measurements of stratospheric aerosol properties at non-volcanic levels. *Atmospheric Chemistry and Physics*, *8*, 983–995.

Thomason, L. W., and T. Peter (editors) (2006), SPARC Assessment of Stratospheric Aerosol Properties, WCRP-124, WMO/TD-No. 1295, SPARC Report No. 4, February 2006.

Thomason, L. W., Poole, L. R., & Deshler, T. (1997). A global climatology of stratospheric aerosol surface area density deduced from Stratospheric Aerosol and Gas Experiment II measurements: 1984-1994. *Journal of Geophysical Research*, *102*, 8967–8976.

Vernier, J.-P., Pommereau, J.-P., Thomason, L. W., Pelon, J., Garnier, A., Deshler, T., et al. (2011). Overshooting of clean tropospheric air in the tropical lower stratosphere as seen by the CALIPSO lidar. *Atmospheric Chemistry and Physics*, *11*, 9683–9696. https://doi.org/10.5194/acp-11-9683-2011

Wang, P. H., McCormick, M. P., Poole, L. R., Chu, W. P., Yue, G. K., Kent, G. S., & Skeens, K. M. (1994). Tropical high cloud characteristics derived from SAGE II extinction measurements. *Atmospheric Research*, *34*, 53–83.

Ward, S. M., Deshler, T., & Hertzog, A. (2014). Quasi-Lagrangian measurements of nitric acid trihydrate formation over Antarctica. *Journal of Geophysical Research: Atmospheres*, *119*, 245–258. https://doi.org/10.1002/2013JD020326

Xu, R. (2001). *Particle characterization: Light scattering methods*. Netherlands: Kluwer Acad., Dordrecht.